UNIVERSIDADE Ð COIMBRA

Ali Payami Golhin

MELHORIA DO DESEMPENHO TRIBOLÓGICO DE REVESTIMENTOS DO SISTEMA WSCF A SECO E EM CONTACTO LUBRIFICADO

Submitted in Partial Fulfilment of the Requirements for the Degree of Master in Tribology of Surface and Interfaces

VOLUME 1

Dissertação no âmbito do Mestrado Conjunto Europeu em Tribologia de Superfícies e Interfaces orientada pelo Professor Doutor Albano Cavaleiro and Doutor Manuel Evaristo e apresentada ao Departamento de Engenharia Mecânica da Faculdade de Ciências e Tecnologia da Universidade de Coimbra

Julho de 2019

Improvement of the tribological performance of WSCF coatings under dry and lubricated conditions

Submitted in Partial Fulfilment of the Requirements for the Joint European Master in Tribology of Surfaces and Interfaces

Author

Ali Payami Golhin

Advisors

Professor Albano Cavaleiro
Doctor Manuel Evaristo

Jury

President	**A/Professor Bruno Trindade**
	Associate Professor at University of Coimbra
Vowel	**Doctor Luis Vilhena**
	Assistant Professor at University of Coimbra
Advisor	**Doctor Manuel Evaristo**
	Assistant Professor at University of Coimbra

Acknowledgements

Abstract

Friction reduction plays a decisive role in energy efficiency; thus, efficient lubrication of the sliding surface is of extreme importance. The combination of low friction coatings with lubricants is the best approach to reduce friction over a wide range of conditions, particularly when lubricant does not respond efficiently and the reduction of friction has to be governed by the low friction coating. However, this approach is not straightforward since the interaction of the coating with the lubricant can lead to worse performance than with uncoated surfaces. The improvement of this interaction by modifying the composition of the coating is the core subject of this research work. For this purpose, coatings of the WSCF system with increasing alloying contents (C and F) were deposited by reactive PVD in an Ar and CF4-discharge atmosphere. The coatings were structurally and mechanically characterised in order to study the influence of adding C and F to the system on the tribological and mechanical properties of the WS_x-based coatings. SEM, WDS, XRD, AFM and Optical microscopy were applied to understand the morphology and structure of the surfaces. The tribological performance of the WSCF system is evaluated in dry and lubricated conditions at different temperatures (RT: 25 °C and HT: 200 °C). According to the results, more alloying elements presented smoother, denser, thicker, and more featureless and amorphous coating. F incorporation in the coatings (up to 9.3 at.%) led to lower coefficient friction and generally better wear resistance due to the higher interplanar distance confirmed by XRD. It is revealed that the influence of alloying elements on the formation of the tribolayers is the mechanism responsible for the difference between the friction coefficients. According to the expectations, it is observed coatings showed the best tribological performance at the dry nitrogen, then at Air-HT compared to the normal Air-RT environment. This study demonstrated that the general tribological behaviour of the high fluorine-doped coating was the best, which suggests alloying WS_x-based layer up to 15.5 at. % C and 9.3 at. % F could enhance the overall performance of these solid lubricants.

Keywords: Solid lubrication, WSCF coating, Fluorine doping, Tribology, Magnetron sputtering

Resumo

A redução do atrito desempenha um papel decisivo na eficiência energética; Assim, a lubrificação eficiente das superfícies em deslizamento é de extrema importância. A combinação de revestimentos de baixo atrito com lubrificantes é a melhor abordagem para reduzir o atrito numa ampla gama de condições, particularmente quando o lubrificante não responde eficientemente, e a redução do atrito deve ser governada pelo revestimento de baixo atrito. No entanto, esta abordagem não é simples, pois a interação do revestimento com o lubrificante pode levar a um desempenho pior do que com as superfícies não revestidas. O melhoramento das interações, modificando a composição do revestimento, é o tema central deste trabalho de investigação. Assim, os revestimentos do sistema WSCF foram depositados com teor em (C e F) crescentes por PVD reativo em atmosfera de Ar e CF4. Os revestimentos foram caracterizados estrutural e mecanicamente para estudar a influência do teor de C e F no sistema com especial atenção nas propriedades tribológicas e mecânicas dos revestimentos à base de WSx. SEM, WDS, XRD, AFM e microscopia ótica foram utilizadas para estudar a morfologia e estrutura dos revestimentos. O desempenho tribológico do sistema WSCF foi caracterizado a seco e em contacto lubrificado a diferentes temperaturas (RT: 25 ° C e HT: 200 ° C). De acordo com os resultados, o aumento do teor em C e F nos revestimentos, resulta numa diminuição da rugosidade, estes apresenta uma estrutura cristalográfica amorfa com uma morfologia de crescimento compacta e sem detalhes. O aumento do teor em F nos revestimentos (até 9,3 at.%) resultou numa diminuição do coeficiente de atrito e uma melhor resistência ao desgaste devido ao aumento da distância inter-planar confirmada por XRD. Observou-se que o mecanismo responsável pelo baixo atrito registado está associado a formação de uma tribo-camada nas duas superfícies em contacto e que desempenho depende da composição dos revestimentos. Observou-se que os revestimentos apresentam melhor desempenho tribológico em azoto seco, depois, em ar-HT, quando comparado ao ambiente normal de RT-ar. Este estudo demonstrou que o comportamento tribológico geral dos revestimentos do sistema WSCF melhora com o aumento do teor em C e F.

Palavras-chave: Lubrificação sólida, revestimento WSCF, dopagem com flúor, Tribologia, pulverização catódica magnetrão

Contents

List of Figures

List of Tables

List of abbreviations

at.%	Atomic percent
AFM	Atomic force microscopy
COF	Coefficient of friction
DC	Direct current
DLC	Diamond-like carbon
EDS	Energy-dispersive X-ray spectroscopy
FEG	Field Emission Gun
GI-XRD	Grazing incidence XRD
HT	High temperature
MoS2	Molybdenum disulfide
PVD	Physical vapour deposition
Rh	Relative humidity
RT	Room temperature
SEM	Scanning electron microscopy
TEM	Transmission electron microscopy
TMD	Transition metal dichalcogenide
WC	Tungsten carbide
WSCF1	$W_{29.5}S_{50.2}C_{10.4}F_{5.3}$
WSCF2	$W_{27.9}S_{44.3}C_{15.5}F_{9.3}$
WSCF3	$W_{25.8}S_{43.9}C_{18.7}F_{8.5}$
XPS	X-ray photoelectron spectroscopy
XRD	X-ray diffraction

Chapter 1 - Introduction

1.1. Industrial problem

Sustainable development regarding limited resources of materials and energy is the major challenge for modern technology. Finding a new source of energy is usually discussed, but another important aspect is the optimisation of using the available energy. During the past decades, the study of the natural phenomena in tribology having benefited strongly with sustainable development [1]. The term tribology is a new field of science, introducing in 1967, however, it is related to the Greek word of tribos which means sliding or rubbing. Friction, wear, and lubrication of materials are the main aspects of tribology. In most cases, they lead to material loss and energy consumption. Reduction of performance and reliability due to surface damage of devices are the main problems of friction-induced wear. In the first case, friction and wear are responsible for roughly one-third of the consumed energy in the industries [2][3].

In order to control these extrinsic properties, it is vital to understand the tribological properties of materials. The main materials of mechanical components in gears and bearings are fabricated from metallic compounds. Regarding Tabor's approach [4], surface interactions between two metallic surfaces could be included bonds first form long-range van der Waals forces in the atomic distance, and as separation distances approach the interatomic distances, would lead to strong metallic bonds. Rabinowicz proposed a general guideline for the selection of materials involving moving contacts [5]. He stated that friction and adhesion should decrease as one progresses from solid solutions to insoluble couples, couples of the same material or metal-nonmetal pairs [5],[6].

Tribological materials are specifically materials designed for friction and wear mitigation. They must meet physical and mechanical property requirements, such as stiffness, strength, thermal expansion, damping, and fatigue life. However, it is almost impossible to balance all of these parameters for tribological components [6]. In practice, lubrication is the primary method of controlling friction and wear. Lubricant materials reduce friction and wear between interacting surfaces by the formation of a protective tribofilm preventing solid/solid contact. They reduce friction between sliding contacts by shearing of the oil molecules across the solid-liquid interface [6].

Liquid lubricants are used in large quantities in industries, not only as lubrication, but also as coolants to prevent the side effect of extreme temperatures and pressures in the interfaces. They are also used in order to decrease the amount of debris and other unwanted particles during various metal cutting and forming processes. However, most liquid lubricants will volatilize at high temperatures and then reacts or condenses on the surfaces, which may damage the substrate. Decomposition products of oils due to higher temperatures can inhibit lubrication effects. Furthermore, liquid lubricants are inappropriate for applications where the liquid can settle and leave some parts unprotected before high-temperature operation [7].

In addition, there are environmental issues associated with the disposal of lubricants, and in many cases, the presence of fluid lubricants is neither recommended nor possible. Therefore, solid lubricants are recommended as the best available option. They are also useful for high-temperature applications due to their low vapour pressure. Moreover, their sublimation does not affect the degradation of the surfaces

[8],[9]. Using solid-lubricant as thin films on bulk materials is a suitable method for reducing wear and friction. In order to prevent the irreversible deformation of the contact surfaces, the friction coefficient in the presence of an effective solid lubricant needs to be less than 0.2 in most applications [10]. These self-lubricating coatings were designed and developed particularly for the food industry and optical systems where fluid lubricant can damage the product. They also can add desired properties to the bulk materials [11],[12].

Transition metal dichalcogenides (TMDs or TMDCs) are layered materials that have long been of interest in solid lubricating. TMDs are used as the surface coating over of a substrate in order to add or enhance some properties to the bulk material. WS_2 is one of the most notable TMDs, which exhibit excellent friction reduction behaviour. Recently, TMDs usually have been doped with different elements. Doping with some elements, including fluorine and transition metal, can improve the performance of TMDs and extend their potential for technological applications [13].

The fluorine is demonstrated to reduce sensitivity to the relative humidity in the tribological investigation of MoS_2 and PTFE (C-F chains) [14]. Other authors reported very good lubrication performances and less sensitive to moisture for a doped $WS_2:CF_x$ films compared to pure WS_2, with great potential for airspace industry applications [15][16].

1.2. Objectives

As it has been mentioned before, the investigation of self-lubricating thin films is an important answer for tribological applications, where using liquid lubricants are not possible or recommended. The overall purpose of this study is to define a step-by-step instruction to investigate the tribological behaviour of a series of self-lubricating thin films based on W and S. This work included systems that had already guaranteed good results in the literature, as well as research that had not so far received much attention. Therefore, this research consists of the current state-of-the-art at the same time as attempting to gain a deeper knowledge of TMDs generally and the shared and differing characteristics of this class of solid lubricants. Specifically, we hope to address the following research objectives:

- What is the influence of carbon and fluorine on the characteristic properties of WSCF coatings?
- Does the fluorine doping improve the tribological behaviour of WSC coatings? How?
- At which coating condition, the best coating properties among the prepared samples could be obtained?
- How is the tribological performance of prepared WSCF coatings regarding different temperatures?

1.3. Scope and thesis organisation

This study aims the improvement of the tribological performance of WS_x-based coatings with the addition of carbon and fluorine. The present thesis is organised into five chapters, which contents are summarised in the following. The introduction and objectives of the thesis are presented in this chapter. State of the art and the background of scientific questions are addressed in the next chapter. The third chapter concerns with the basis of the methodology of experimental evaluation. The results are presented and discussed in chapter five, and finally the conclusions are listed in the last chapter.

Chapter 2 - **State of the art**

In this chapter, we first discuss the solid lubricant coatings and lubrication mechanisms, their applications and types. Accordingly, we focus on the structures of the TMDs, describe the fundamental, TMD-based coatings, performance, and then we have addressed the knowledge above of the WS_x-based coatings and a discussion about the doping of TMD films.

2.1. Solid lubricant coatings

New challenges in lubricants design such as high loads, high temperatures, high speeds, and high contact pressures, require new lubrication systems to function properly under extreme working conditions [17]. Solid lubricants are critically important for safe and smooth operations of many mechanical systems at different conditions, where the primary target is to reduce kinetic friction and wear. The well-known solid lubricants are diamond and DLC films, lamellar solids, lubricious oxides, and soft metals [18].
The process of sliding surface asperities against each other is called kinetic friction. Solid lubricants separate the interacting surfaces to decrease the friction. They are effective, especially at high loads and temperatures, where kinetic friction increases due to the lack of liquid lubricants in the contact surfaces. Therefore, solid lubricants are one of the best options in many applications at high-load and elevated temperatures [19].
Graphite, WS_2 and MoS_2 are widely applied as solid lubricants [19]-[21]. The lubricating effect in this type of coatings is related to the weak van der Waals force between two adjacent layers of these structures, which allows adjacent layers to slide easily against each other due to their relatively low shear strength. While, because of covalent bonding among atoms in the same atomic layer, the layer structure shows high modulus and strength. It allows them to decrease the friction between two surfaces [22]. Accordingly, the requirements of an appropriate solid lubricant are [19]:

- Good adhesion of the solid lubricant coating to the substrate, particularly at high shear stresses.
- High compression strength perpendicular to the sliding direction. This property provides a coating capable of withstanding high loads.
- Low shear strength in the sliding direction. A good solid lubricant shows a low coefficient of friction because of the easy shear movement of the lubricant material.

The best combination of the last two properties possesses anisotropic materials such as graphite, WS_2 and MoS_2 having a lamellar crystal structure. Based on the above requirements, the advantages and disadvantages of solid lubricants are summarised in Table 1.

Table 1: Advantages and disadvantages of solid lubricants [23].

Advantages	Disadvantages
▪ Ability to work under high loads	▪ Finite wear life
▪ Stable in high-temperature	▪ Adherence
▪ The diversity of the application forms	▪ Fluctuation in friction coefficient
▪ High heat dissipation with high thermal conductive lubricants	▪ Complex deposition procedures
▪ Highly cryogenic temperature, vacuum, and high-pressure environments	▪ Tribo-reactivity
▪ Enable equipment to be lighter and simpler because lubrication distribution systems and seals are not required	▪ Higher coefficient of friction and wear as compared to hydrodynamic lubrication
▪ Resistant to deterioration in high radiation environments	▪ Poor heat dissipation with low thermally conductive lubricants Low stability of the lubrication film
▪ Resistance to abrasion in high-dust environments	▪ Less convenient system of the lubricant delivery to the friction surfaces, while fluid lubricants are continuously supplied, filtered, and cooled
▪ Resistant to deterioration in reactive environments	▪ Poor self-healing properties so that a broken solid film tends to shorten the useful life of the lubricant
▪ Offer flexibility in locations where access for servicing is difficult	
▪ More effective than fluid lubricants at high speeds	▪ May have an undesirable colour

Accordingly, corresponding requirements of solid lubricants to overcome the present limitations are [19]-[23]:

- Heat dissipation
- Interface optimisation
- Difficulty of replenishment
- Effect of temperature and environments
- Run-in control and wear debris removal
- Lowering costs

2.2. Application

Wear mechanisms vary with load and pass frequency; therefore, materials should be selected regarding their applications. In modern applications, solid lubricants are often used as thin solid films on sliding surfaces. Research into solid lubricants, particularly layered TMDs such as WS_2, has become extensive, involving fields as diverse as spintronics, catalysis, lubrication, optoelectronics, and energy storage [23]. Generally, typical applications of solid lubricants are conditions when liquid lubricants are inappropriate such as sliding or reciprocating motion. In these conditions, conventional lubricants are squeezed out. Likewise, they are useful when chemically active lubricant additives have not been found for particular contact surfaces, for example, ceramics and polymers. In this case, solid lubricants can prevent galling and fretting corrosion. The lamellar structure of solid lubricants leads to high bearing-load resistance combined with low shear stress. They cover most applications in metal forming as they involve persistent plastic deformation [24].

In addition, they can support the high-temperature process. Two examples of applications at elevated temperature are high-speed machine tools and airfoil bearings for aerospace engines. Both applications involve intermittent high loading and high pass frequency compared to constant high-speed contact with relatively low loads for machine tools [10]. The uses of solid lubricants are expected to further increase in the future since the operating conditions of tribosystems are becoming more and more challenging regarding technical aspects and environmental concerns [24].

2.3. Types

Generally, there are two categories for solid lubricants, including intrinsic and extrinsic types. In intrinsic type, atomic structure shears easily to facilitate interfacial sliding (e.g., MoS_2 and WS_2). In extrinsic type, the influence of an additive from the surroundings to activate a low shear mechanism is important, e.g., graphite, as it needs to be terminated with water or another condensable vapour [10][19].

Solid lubricants for application at high temperatures may be divided into three categories of metal oxides (e.g. V_2O_5, $Ag_2Mo_2O_7$), fluorides (e.g. CaF_2, BaF_2, and CeF_3) and soft metals (e.g. Au, Ag, Cu, In, and Pb). Most solid lubricants that operate at low temperatures (25 to 300 °C), does not show good performance at higher temperatures (higher than 300 °C) due to their oxidation. They become abrasive, and therefore, lose their lubricity. All of these three types of solid lubricants plastically deform and/or form low-shear-strength surfaces at higher temperatures [10]. Solid lubricants can be either a single-phase or multi-phase composites. The single-phase type consists of elements or compound materials. Accordingly, they are divided into four main types, including [6]:

- Carbon-based materials (e.g., DLCs, graphite, and nanocrystalline diamond)
- Soft metals (e.g., gold, silver, tin, and indium)
- Polymers (e.g., PTFE)
- Transition metal dichalcogenide compounds (e.g., MoS_2 and WS_2)

Despite polymers, other solid lubricants can form as thin films for tribological purposes.

2.3.1. Carbon-based materials

Among carbon-based material, graphite and DLC are a well-known classic example of solid lubricants. Despite graphite, DLCs are naturally amorphous. DLCs are synthesised, particularly in the reduction of friction and wear [6].

2.3.2. Soft metals

Some soft metals such as silver (Ag), lead (Pb), tin (Sn), bismuth (Bi), and cadmium (Cd) possess lubrication properties. Because of their low shear strength and high plasticity, their coatings on relatively hard substrates may result in low friction ($\mu \sim 0.1$). They are used either in pure form or as bearing alloys in coatings produced by the methods of vapour deposition, electroplating, and thermal spraying. Casting or sintering methods are used in their composites. Soft metals are widely used in high-temperature applications up to 1273 K and in engine bearing materials [6],[24].

2.3.3. Polymers

Molecular profile and low intermolecular cohesion of some polymers, make them as good solid lubricants. PTFE, specifically, is the most useful polymeric materials well-known for its anti-friction property. It consists of carbon and fluorine atoms, and widely used as an additive in lubricating fluids. PTFE cannot easily be polarised since it has not unsaturated bonds. At low contact stresses (7.3–73 MPa), it forms a chemically stable thin transfer film on the counter face during sliding. PTFE alone is unable to add the desired combination of low friction and wear to the surface. Despite other solid lubricants, PTFE is not a layered structure, and its operating temperature is limited to 260 °C. It possesses low surface energy, low thermal conductivity, colourless film lubricity, low load-carrying capacity, very low coefficient of friction at low loads, good chemical resistance and good sliding-friction reduction [6],[24].

2.3.4. Transition metal dichalcogenides

Among various solid lubricants, TMD materials are especially attractive due to their outstanding tribological properties. Although graphene and transition metal oxides studied extensively in the past decade, TMDs scientifically and industrially attractive in solid lubrication materials [26]. TMDs, such as MoS_2, $MoSe_2$, WS_2, and WSe_2, are materials that have long been of interest, and with the advent of modern synthetic methods, it has become possible to modify them according to the tribological system. The compounds MoS_2 and WS_2, are well known of the TMD family of compounds. They are naturally occurring minerals molybdenite and tungstenite, and are widely used in several applications. Their excellent friction reduction capabilities are the result of the weak van der Waals forces operating between the layers [13]. However, sensitivity to humidity as the main limitation of these TMD-based lubricants can significantly restrict their applications [19]. Fundamental properties of TMDs, along with their performance is discussed in the following section.

2.4. Fundamental properties of TMDs

TMDs are layered materials with strong in-plane ionic-covalent interactions and weak out-of-plane van der Waals bonds, enabling them to be mechanically exfoliated. They may be considered as a stack of triple layers similar to graphite, where a transition metal layer, which has a hexagonal lattice structure, is sandwiched between two chalcogen layers. The transition metals are elements of group IV (Ti, Zr, Hf), group V (V, Nb, Ta), or group VI (Mo, W) and chalcogen atoms are S, Se, and Te. Polymorphism is one of the unique features of TMDs. The stoichiometry of metal dichalcogenides is MX_2, where M stands for the transition metal element, and X represents a chalcogen. MoS_2 and WS_2 are the most common representative TMDs, which has garnered a great deal of research interest [17],[27].

Fig. 1 represents the general structure of TMDs and structural polytypes of them, including one tetragonal (1T), two hexagonal (2H), and three rhombohedral (3R). The inter-layer spacing between the bottom and top chalcogen layers of two neighbouring layers in various TMDs is about 3.6 Å, while, in-plane lattice constants are between 3.1 Å for VS_2 to 3.6 Å for $TiTe_2$ [27].

Each of the three phases in Fig. 1 has its property. The octahedral (1T) is well conductive but metastable, the trigonal prismatic (2H) is poorly conductive but stable, and the rhombohedral (3R) is nearly insulator [28]. MoS_2 and WS_2 as Mo^{4+} and W^{4+} have comparable Shannon Prewitt crystal radii (0.790 Å vs 0.800

Å), as they often adopt the same hexagonal parent structure, and, it is possible to form a continuum of compositions of Mo_xW_x-$1S_2$ for $0 \leq x \leq 1$ [29].

Notwithstanding, the weak interlayer interactions, the surface relaxation effects in thin-film TMDs are significant. For instance, the interplanar spacing between Molybdenum and Sulfur atoms at the surface is 5% smaller than that in bulk. This effect has an important influence on the property of the thin film, specifically phonon frequencies[19].
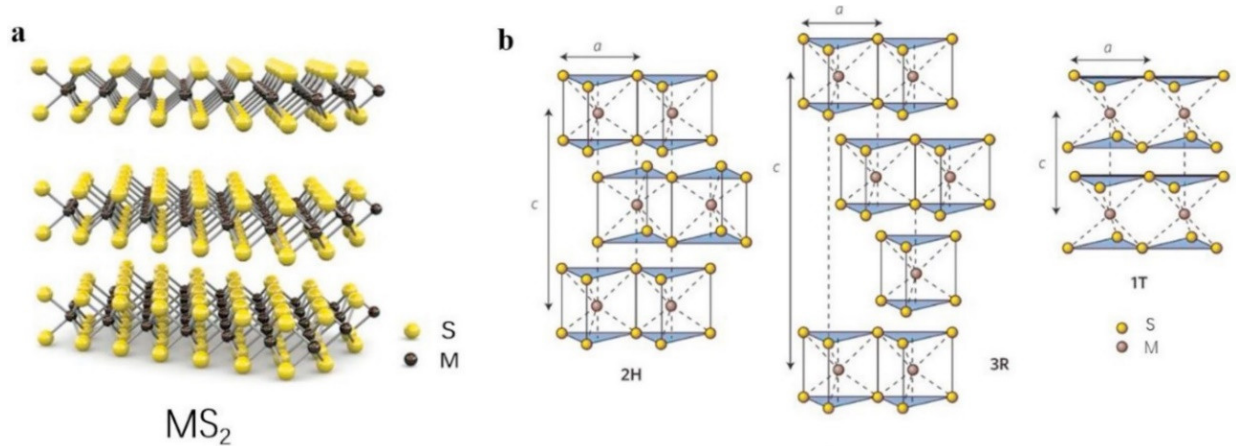
Figure 1: a) Crystal structures of TMDs. b) Three structural polytypes of MoS_2 and WS_2, 1T structure, with tetragonal symmetry and octahedral coordination; 2H structure, with hexagonal closed packing and trigonal prismatic coordination; and 3R structure with rhombohedral symmetry [27].

Non-local van der Waals interactions are not the only source of interlayer bonds in layered TMDs, and Coulombic interactions are important too. These forces determine indirect to direct band gap transition that occurs in very thin TMD coatings, especially in a single layer [19]. Similar to graphite, the weakness of intermechanical bonds is intrinsic to their crystal structure. In the case of WS_2, a sheet of tungsten hexagonal atoms is sandwiched between two hexagonally packed sulphur layers. The bonding within the S–W–S is covalent, and the weak van der Waals bonds between them enable the ability of intracrystalline slip in the structure and transfer film formation on the counterface in order to accommodate interfacial sliding. Thus, the lubrication mechanism in TMD consists of three phases [30]:

I.   Creation of (0 0 0 2) basal planes
II.   (Re)orientation parallel to the sliding direction
III. Development of a transfer film on the rubbing counterface

The ability to transfer films on the counterface in TMDs implies that coating one contacting surface would suffice to generate initial lubrication in a tribosystem after the run-in period. Furthermore, consideration of fully crystalline TMD films or the direction of the preferred crystallographic texture of (0 0 0 2) basal planes regarding the sliding direction is not necessary. In this case, it is reported that frictional stresses can induce crystallinity into the TMD films and resulted in a reorientation of the basal planes in as-deposited crystalline films [31]-[33].

Both MoS_2 and WS_2 coatings exhibit long wear life (several million sliding cycles) due to their extremely low friction coefficients ($\mu \sim 0.05$ or less). It is not important whether they are employed in either ultra high vacuum or dry inert gas as they preserve their intrinsic lubrication behaviour. However, sliding in humid air leads to unsaturated bonds or dangling on the edge of basal planes reacting with oxygen forms

triooxidation products (e.x. MoO_3 or WO_3). It results in higher friction coefficients (0.15–0.2) and consequently short wear life. In elevated temperatures, while MoS_2 begins to oxidise higher than 300 °C, WS_2 is stable up to about 400 °C, indicating that WS_2 has better thermal stability [13].

Other TMDs, such as ditellurides and diselenides of Mo and W, have a similar structure to MoS_2 and WS_2, are of little technological interest, as their lubrication performance is not proved yet. The humidity of the atmosphere may negatively affect the tribological performance of MoS_2 and WS_2 coatings [13]. MoS_2 and WS_2 have a hexagonal P63/mmc structure and a considerable band gap that gives them unique properties, such as the high density of active sites along edges and large surface area, which allow them to be used in a wide range of applications including electrochemical reactions. Due to this structure, another important application of TMD-based materials is composite structures, which make them similar to carbon nanostructures [19]. Therefore, there is significant potential for commercialisation in the future [34].

2.5. WSC coatings

Pure TMD coatings, such as WS_2 thin films, cannot withstand in the harsh industrial applications due to their weak tribological behaviour, insufficient load-bearing capacity and toughness, low hardness, and low adhesion to the substrate [35]. Similar to other TMDs, WS_2 usually has a porous and columnar morphology [36]. Therefore, materials and compounds are added to WS_2 coatings to enhance their mechanical and tribological properties. For instance, Fig. 2 illustrates a schematic of conventional designs of WS+C films.
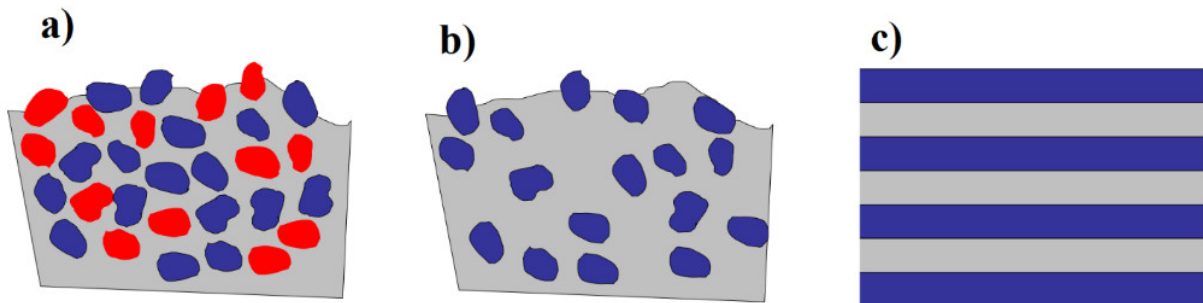
Figure 2: Schematic of conventional designs of WSC films: a) Embedded WC nanoparticles and WS_2 nanograins in a nanocomposite coating with an amorphous carbon matrix, b) Nanograins of WS_2 in a carbon matrix, and c) The super-lattice WS_2+C layers in the coating [37].

Polcar et al. showed that alloying with Nitrogen lead to a fully amorphous WSN film, which had lower contaminants [36]. Gustavsson et al. indicated the positive effect of alloying on the quality of the coating both in less porosity and high hardness [38].

Using carbon in TMDs was studied first by Voevodin et al. [39], where they investigated the combination of solid lubricants of WS_2 and hard WC phases in a nanocomposite with an amorphous carbon matrix.

Alloying WS_2 films by carbon is proved can provide a considerably better coating with higher tribological performance, adhesion to the substrate, and increasing the hardness of the film by Zabinski et al. [15]. Nossa et al. [40] confirmed the positive role of the third element, including C and N, on the enhancement of mechanical properties in W-S solid lubricant systems.

2.6. Doping of TMD films

In order to maintain the excellent lubricity of TMDs in harsh environments, a wide range of methods have been attempted. Using additives to make TMDs composite coating is the most common method. For this purpose, doping with elements such as Ti, F, Pb, Au, Cr, Cu, and Zr are proved to have a positive influence on these coatings [41][42]. The presence of these dopants can enhance coating hardness, density, and oxidation resistance compared to pure TMDs. The dopant element avoids the growth of the columnar structure in TMDs and hinders the formation of defects, as well as large grains in the films [8].

Among the dopants, Sb_2O_3- and Au-doped MoS_2 nanocomposite coatings and other doped MoS_2 and WS_2 thin films are gaining acceptance as robust coatings for commercial use [18]. The performance of other TMDs such as $NbSe_2$ and $TiSe_2$ has been more recently reported to present satisfactory after doping [43],[44].

As referred previously, doping can modify the morphology of coating, and transition metal doping offers a strategy for the activation of the surface as another way of increasing the density of catalytically active sites. However, doping may make it unsuitable in some applications. Therefore, the ability to synthesise large crystals and thin films of TMDs with controlled composition is potentially important in the aspect of technological use. In this regard, the crystal radius of the dopant and its oxidation state are also important factors. Because in some cases it is desirable to iso-electronically and isomorphically substitutes for the transition metal, although it can also be efficient to induce defects, vacancies, or alter the structure of parent. For instance, tungsten-doped MoS_2 shows a higher specific capacitance compared to pure MoS_2 for the same active weight, and the amorphous carbon supported material possess the highest specific capacitance [13].

In this case, co-sputtering of MoS_2 and the dopant Ti target in an unbalanced magnetron sputtering process yielded coatings of MoS_2 doped with almost 16 at. % Ti, which were substoichiometric concerning the content of sulphur [45]. Similarly, another research has investigated doping of WS_2 with Ti produced by DC magnetron sputtering, and it is reported that the optimal level of Ti for low friction at room temperature is 7 at. % [6]. However, the coefficient of friction was not as low as for pure WS_2; the wear lifetime has been proven significantly increased. High levels of Ti (more than 33 at. %) caused amorphous coatings along with compromised friction reduction properties. The authors suggested that increasing amounts of Ti resulted in a reduction of the crystallinity of the coating. It was consistent with the dopant disrupting the structure rather than directly substituting for tungsten [6].

Ti-doped MoS_2 showed having minimal "cophonicity", which were observed for WTe_2 and WSe_2 if Ti is substituted for Mo in the lattice, as it provides a route in the reduction of the frequency of vibrational modes associated with interlayer sliding [46]. WS_2 coating doped by Zirconium has been coated on a variety of substrates and exhibited the lowest wear rate, the lowest coefficient of friction, and the highest hardness comparing pure WS_2 in an unlubricated interface in sliding wear tests [47].

In particular, the main issue of doping of WS_2 is the problem between their layered structures and elements that exhibit competing bonding coordination. In another word, a major technical hurdle needs to be addressed form 3D structures as opposed to layered structures. Careful selection of dopants, the methodology of synthesis of the film and the concentration dopant can alter the properties of TMDs in different ways, such as those discussed above molybdenum disulphide and tungsten disulphide [6].

These properties include the introduction of magnetic properties (Mn, Fe, Co, and Cu), alteration of the intrinsic n-type semiconducting behaviour to p-type (Nb), changing the morphology of the alloy product, and enhancing of catalytic properties for industrially important reactions, such as hydrodesulfurization (Co), hydrogen evolution (V and Re), and the reduction of carbon dioxide to methanol (Co). These modifications can alter the edge site populations for catalysis, change surface area and affect the delivery

of lubricating particles in tribosystems. Sputtering based doping methods can improve the wear resistance of thin films through dramatical modification of the structure of the coating [6],[19].

It has also been observed that WS_2 film doped with some elements can be typically bear the harsh tribological environment. Multiple papers have confirmed the effectiveness of doping on TMDs, however, the parameters influencing their tribological performance have not been fully revealed. In fact, there is a lack of comprehensive reports about additives in the solid lubricants [48][49].

For instance, while several metals or oxide dopants in MoS_2 and WS_2 have been successfully studied, fluorine is rarely reported in the research related to TMDs. In addition, the fluorine-doped solid lubricants such as C-F or F-DLC sputtered coatings are reported to deteriorate the hardness and the elastic modulus of the thin film [50]. Conversely, doping WS_2-based coating with F (WS_2:CaF_2 coatings) indicated has excellent lubrication performances (COF = 0.15) at high temperature (500 °C), which is suitable for aerospace applications [16].

Although numerous engineering applications require solid lubricants in un-lubricated contacts, it is a common application that uses them in conjunction with liquid lubricants. For instance, doped DLC coatings with liquid lubricants are used to enhance the performance of gears, bearings, and magnetic hard disk drives. Doped TMDs, are often used in bushings, satellite components, gears, and shafts as low friction coatings [6].

The economic aspect of adopting a new paradigm for replacing a current lubrication technology rather than facilitating a new one is an important factor, which should be considered in cases where doped TMDs are candidates for adding to the conventional tribological systems. Expensive raw materials or rarely find elements are the potential barrier, especially when the current technology is affordable and/or convenient. Therefore, the benefits of doped TMDs must offer long-term sustainability considering the unpredictable availability and cost, and at last but not least, their environmental impacts. In this regard, doping can help not only in the improvement of tribological and mechanical behaviour but also in the decreasing materials consumption and hazardous materials disposal through a controlled deposition process [13].

Generally, literature is scarce on the mechanical properties of fluorine-doped TMDs, especially carbon-contained TMDs. Therefore, a study on the alloying of the WS_x-based solid lubricants via F and C is still missing. In this research, this type of solid lubricants films is studied to improve the tribological and mechanical properties performance of the coating [13].

Chapter 3 – Methodology

In this chapter, a brief description of the experimental method of deposition procedures followed in this study is given. Regarding the characterisation of the coatings, several microstructural analyses were performed by AFM, X-Ray and Electron Microscopy -based techniques to study the microstructure, chemical composition and morphology of the coatings. The tribological behaviour was studied using ball-on-disk. In addition, nanoindentation and scratch test was used to investigate the mechanical properties of thin films.

3.1. Deposition procedure

The main methods of synthesizing solid lubricants and TMDs are physical vapor deposition (PVD) techniques including DC and RF sputtering, pulsed laser ablation, ion beam deposition, evaporation, burnishing, impingement of coatings, chemical vapor deposition (CVD) techniques including metal-organic CVD, microwave plasma CVD, plasma-enhanced CVD, and atomic layer deposition (ALD) [6]. PVD and CVD as the "bottom-up" strategies, were used in the fabrication of pure TMDs, including MoS_2 and WS_2, and they are appropriate for doping the TMD-based solid lubricant [28].

The PVD processes are more attentive for WSC coatings because this method can be refined to control the size and number of layers in the materials, which is particularly important given the thickness-dependent properties [51]. These techniques produce thin films in composite, gradient, nanostructured, duplex, and multiplex, forms, resulting in better durability and tribological performance in the harsh environment. Recently, several papers discussed designed "adaptive" or "chameleon" solid lubricant coatings to adapt to the changing conditions of tribological applications. Several PVD techniques are now available for the deposition of W-S coating on various kinds of substrates, such as ceramic, metallic, and polymeric substrates [24].

One of the best deposition techniques used for deposition of TMDs is DC magnetron sputtering technique [24]. Not only as a method for PVD technique but also sputtering is used for cleaning surfaces. In this method, a solid target is placed in a chamber filled with an inert gas like Argon. The gas is ionised by using a strong electric field and change into the accelerated plasma stream. These high energy ions in the plasma hit the target and based on their kinetic energy, some atoms of the target are ejected. Consequently, these atoms will go to the substrate and will form the thin film physically. The probability of electron ionisation can increase using magnetrons in the deposition chambers [6].

In magnetron sputtering, magnets behind the target provide a denser plasma in front of the target and improve the efficiency of sputtering. The operation modes for magnetron sputtering are direct current (DC), radio-frequency (RF- or pulsed DC). The target material in DC sputtering should be electrically conductive to prevent rising positive charges at the cathode surface, which has a negative influence on the sputtering process. In RF sputtering, the conductivity of the target is not important [6][52].

An alternative method for depositing insulators is using reactive sputtering, which the target is metallic material and insulator is in the reactive form. This method provides faster and higher deposition rates for

insulators. DC power can be used for obtaining reactive depositing insulator. This process has better deposition rates and sputter yields compared to RF sputtering; however, the disappearing anode and arcing are the main problem of this deposition technique [53].

Structural, morphological and chemical characteristics of W-S films depend on the sputtering method and deposition parameters. The composition and thickness of layers of the coating can be controlled using different targets and deposition parameters including time, temperature, distance and the shape of the target, controller of the electric field etc. [6][37]. A schematic of reactive DC magnetron sputtering equipment is illustrated in Fig. 3.
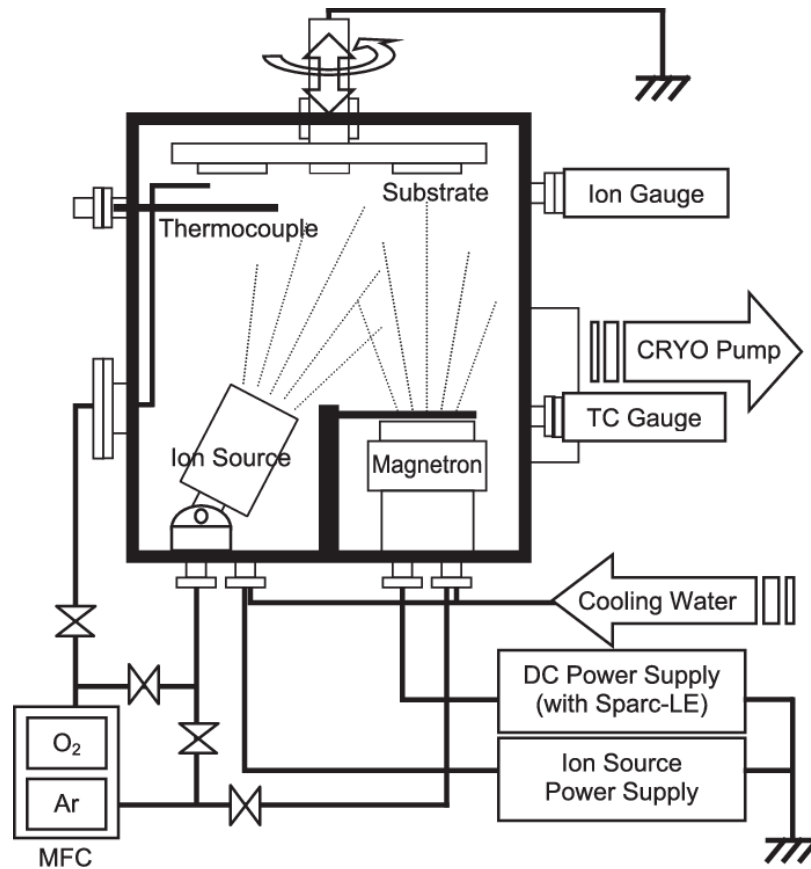
Figure 3: The reactive DC magnetron sputtering system [54].

In the WSCF deposition procedure, the Cr target acts as the interlayer source, which plays a key role in increasing the adhesion of the WSCF coating on the substrate. In this work, the ratio between Cr and WS_2, C and F on the surface and sample compositions is controlled by the individual powers applied to the targets, the number of pellets and controllers on the sputtering equipment.

In this study, the WSCF coatings were deposited by a DC reactive magnetron sputtering on mirror-polished (1 0 0) Si wafers for analytical purposes, and 100Cr6 and M2 steel disc substrates for mechanical testing. The hardness of 100Cr6 and M2 steel samples was close to 5 and 9 GPa, respectively. M2 High-Speed Steel (M2) is tungsten-molybdenum high-speed steel, and 100Cr6 is a chromium molybdenum high carbon steel. Both of them are widely used to manufacture mechanical components due to its well-balanced toughness, wear-resistance and hardness properties. Chemical composition of steel substrates is presented in Table 2.

Table 2: Chemical composition and percentage of elements of steel discs [55].

Element	C	Mn	P	S	Si	Cr	V	Mo	W
M2 regular C steel (wt.%)	0.78-0.88	0.15-0.4	Max. 0.03	Max. 0.03	0.2-0.45	3.75-4.5	1.75-2.2	4.5-5.5	5.5-6.75
100Cr6 steel (wt.%)	0.93-1.05	0.25-0.45	Max. 0.025	Max. 0.015	0.15-0.35	1.35-1.60	-	Max. 0.10	-

The steel substrates were mechanically polished by SiC sandpapers, with increasing grit size from 120[#] to 2000[#] on the automatic metallographic grinding and polishing machine (model RotorPol 21 by Struers with 25 cm plate diameter). In order to further reduce surface roughness, the polishing procedure is followed using a diamond paste of particle size down to 3 μm. Before the deposition, the substrates were ultrasonically degreased in acetone and ethanol baths for 15 min, and, then, air-dried to remove undesirable contaminants from the surface. The coatings deposition was conducted in a vacuum chamber from WS_2, Cr and C targets using a semi-industrial deposition equipment model TEER Coating Limited equipped with four cathodes. Fig. 4 shows the inside of the chamber before the deposition of coatings.
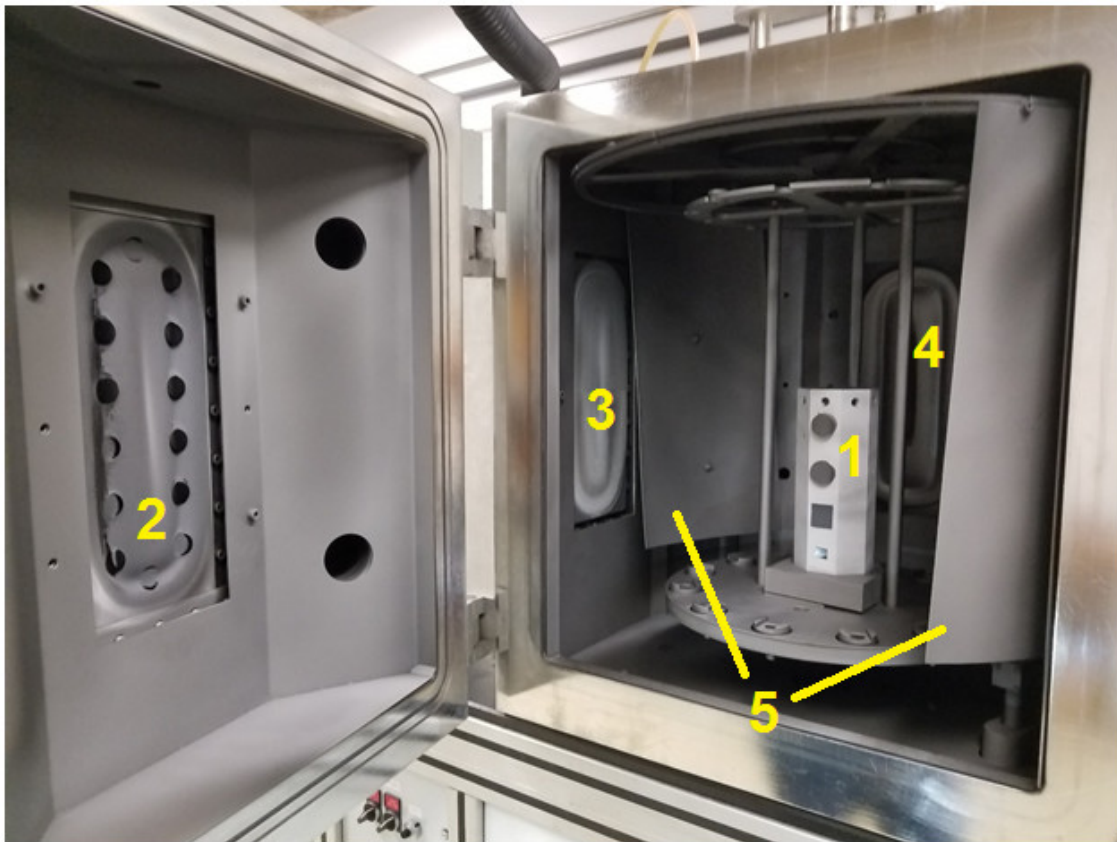
Figure 4: Setup of the substrate holder for deposition inside the DC reactive magnetron-sputtering chamber: Sample holder (1), Cathodes (2, 3 & 4) and rotating shutter panels (5).

In a vacuum chamber (275 dm^3 volume capacity), the substrate holder vertically placed at 30 cm distance with oppositely pair-paralleled targets (380*175*10 mm^3) under rotation in the centre (Fig. 5). The rotation speed was high enough (20 rev/min) to avoid a multi-layered structure growth.
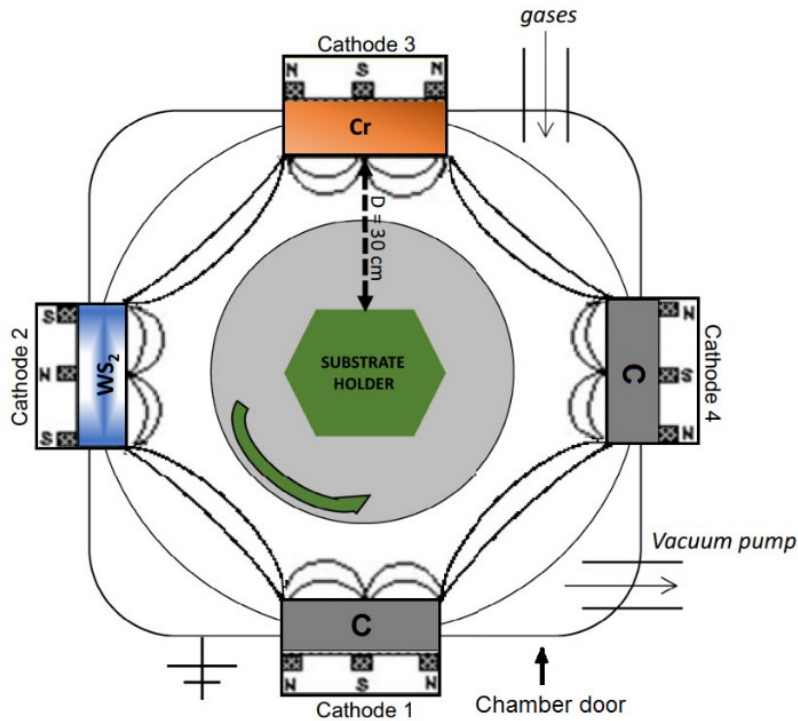
Figure 5: Schematic of the three-target magnetron sputtering for the deposition of the WSCF coatings.

The chamber before the deposition procedure was pumped down to 10^{-5} Pa by using a primary and a diffusion pumping system. The substrates and the targets inside the chamber were sputter-cleaned simultaneously by plasma etching for 20 min. The 1000 W applied power in each cathode provided the argon plasma atmosphere (0.37 Pa) around the substrate electrode.

Three different WSCF coatings were deposited in order to investigate the influence of alloying elements on the tribological behaviour of WS-based TMD films. The prepared samples named WSCF1 (as a reference), WSCF2 and WSCF3, the deposition conditions are listed in Table 3. Other coating parameters, including applied power on WS$_2$ and Cr cathodes and flow rate of Ar and CF$_4$ remained constant for all samples.

Table 3: Deposition parameters for WSCF coatings.

Sample	Cathode 1: C (W)	Cathode 2: WS$_2$ (W)	Cathode 3: Cr (W)	Cathode 4: C (W)	Gas Pressure (sccm)	
					Ar	CF$_4$
WSCF1	0	1500	2000	0	50	4
WSCF2	250	1500	2000	250	50	4
WSCF3	500	1500	2000	500	50	4

During the deposition process, the substrates were mounted on a rotating substrate holder, passing each target alternately. The adhesion of the coating to the substrate is improved by deposition of a chromium

interlayer on the substrates by with a 2000 W power applied on the Cr cathode before the coating deposition. The details of the steps used to deposit the samples are summarised in Table 4. During the target and substrate cleaning, the shutter is in front of the target to avoid cross-contamination of both.

Table 4: Deposition procedure in the chamber.

Step	Process time (min)	Flow rate (sccm)		Shutter rotating angle (°)	Applied power (W)
		CF4	Ar		
1- Cleaning C2 & C4	20	0	35	-	C2&C4: 1000
2- Cleaning C1 & C3	20	0	35	90	C1&C3: 1000
3- Deposition of Cr interlayer	10	0	35	90	C3: 2000
4- Preliminary gradient deposition of WSCF coatings	10	0 -> 4	50	45	C3: 2000 -> 0 C2: 0 -> 1500 C1&C4: 0 -> 0(WSCF1), 250(WSCF2), 500(WSCF3)
5- Main deposition of WSCF coatings	10	4	50	45	C3: 0 C2: 1500 C1&C4: 0(WSCF1), 250(WSCF2), 500(WSCF3)
6- Cooling in the chamber	10	0	50	-	All zero
Cathode 1&4 (C1 & C4): carbon; Cathode 2 (C2): WS_2; Cathode 3 (C3): Chromium					

3.2. Characterisation and evaluation

3.2.1. SEM/WDS

The thickness of the WS_2-based films will usually be a few μm based on the previous studies, thus, optical microscopy cannot reveal the structure and morphology of the coating. In order to study the microstructural characterisation and film thickness in detail, SEM technique should be considered. In SEM, an electron beam is emitted to the sample surface, provides information on the composition and topography of the surface. Generally, secondary (SE) and backscattered electrons (BSE) provide in-detail images of the sample surfaces to examine the fracture cross-section and surface morphology of the films. Based on SE images, topographical contrast can be obtained, and BSE images give atomic number contrast. Wavelength dispersive spectroscopy (WDS) in SEM equipment is a precise analysis technique to reveal the chemical composition of the sample. It is a non-destructive quantitative analysis, which can detect elements from atomic number 5 (boron) and higher. Compared to EDS, WDS exhibits superior sensitivity of trace elements [56].

In this method, a single WD spectrometer typically mounted on an SEM instrument horizontally. In another method, known as EPMA, up to five spectrometers may be mounted vertically around the sample chamber in sequence. In WDS technique, X-rays are produced by exciting an atom. Then it is focused through a crystal spectrometer to a detector, and converted to photoelectrons, which in turn generate an electrical signal proportional to the chemical composition of the sample [57].

SEM is used for determining morphology and thickness of the film across its cross-section. In order to perform SEM analysis, a high-resolution Zeiss (Merlin-61-50) equipment, with charge compensation and equipped with a FEG (Fig. 6). The coatings on silicon substrates had already been cleaned and put inside of the equipment. SE detectors were used to investigate at different magnifications, and images are captured at these magnifications. In order to see the morphology and compactness of coatings, samples were studied in a planar way, and cross-sectional imaging was considered for investigation layers and the thickness of the coating [56].

In this study, SEM and WDS tests were implemented on the silicon wafer samples. Specimens up to 200 mm in diameter and up to 50 mm in height can be readily accommodated in a large-chamber SEM. After WDS, it is possible to capture better SEM images due to the high vacuum in the chamber.

Figure 6: The SEM instrument equipped with WDS detector used for studying morphology and chemical composition of samples.

In order to determine the chemical composition, an Oxford Instruments WDS detector was used at 5 mm WD, 15 kV acceleration voltage, and 3 iterations. The SEM column and sample chamber were at a moderate vacuum to allow the electrons to travel freely from the electron beam source to the sample and then to the detectors. It took about half an hour to reach the desired vacuum state in the chamber. High-resolution imaging is done by the chamber at a higher vacuum, typically from 10^{-5} to 10^{-7} Torr. The microscopy was done from lower to higher magnification. The SEM micrographs were captured in two various areas in order to check the homogeneity of the coating along the surface of the coating. In each region, the images were taken in 25 KX and 50 KX magnifications. The cross-section of the sample has been analysed in the range of 15 KX to 40 KX. The accelerating voltage was 2 kV, and the working distance was in the range of 5.0 to 6.5 mm.

3.2.2. XRD

XRD is a rapid and non-destructive analytical technique primarily used for phase identification of crystalline material. XRD provides reliable information about the crystallographic structure of coatings and determines the preferred orientation of the films. It can yield the unique fingerprint of Bragg reflections associated with unit cell dimensions. Since the properties of a material can often be linked back to the

arrangement of atoms in its crystal structure, it helps to determine the atomic and molecular structure of a crystal, distinguishing between amorphous and crystalline material and quantification of the percent crystallinity of a sample [58].

Bragg's Law defines the relationship between the wavelength of an X-ray beam and the distances between reflecting planes in a crystal structure, which is called diffraction, by the following equation

$$n\lambda = 2d_{hkl} \sin(\theta)$$ Equation 1: Bragg's law

where λ is wavelength (nm), n is an integer order, d is the lattice spacing (nm), and θ is the angle of incidence or scattering angle [59].

Constructive interference of diffracted X-ray beams occurs based on Bragg´s Law. Consequently, a `Bragg reflection´ will be picked up by a detector scanning at this angle. The interlayer spacing of atoms in the crystal structure can be obtained by positions of these reflections, which allows the identification of phases within a given sample. Peak intensities determine the presence of a particular atom in the structure and the amount of contribution of a specific reflection in X-ray scattering. In addition, it may be possible to quantify each phase present, the crystallinity of a sample crystalline structure, strain and size, and their lattice parameters; all important information in material characterisation and quality control. For a single crystal, a single wavelength can satisfy the Bragg's law. Regarding a single orientation of the crystal to the main beam, rotation of the crystal will bring planes into the Bragg condition [58][60].

XRD can be used for a wide range of samples. The best results will be achieved by more crystalline samples. Thin films deposited on a substrate, solid samples and small volumes of sample taped on microscope slide glass can also be used but will have varying degrees of effectiveness. In practical terms, amorphous materials never have peaks in diffraction patterns using X-rays. They can show an amorphous bump, but it would be very broad. The extra peak in the pattern is coming from a crystalline phase [60],[61].

The standard XRD measurement is the $\theta - 2\theta$ mode, which measures only the reflections from the lattice planes parallel to the surface. Unlike powder samples, all reflections may not be observed for the WS_2-based coatings since grains with random orientations usually do not present on the surface. In this case, the GI-XRD mode can enhance the received signals from the coatings through keeping a constant small incidence angle (less than 5°, usually in the range of 1° to 3°) while scanning the detector (Fig. 7). Grazing incidence is considered in the analysis of the coating when the X-ray cannot penetrate into the substrate.
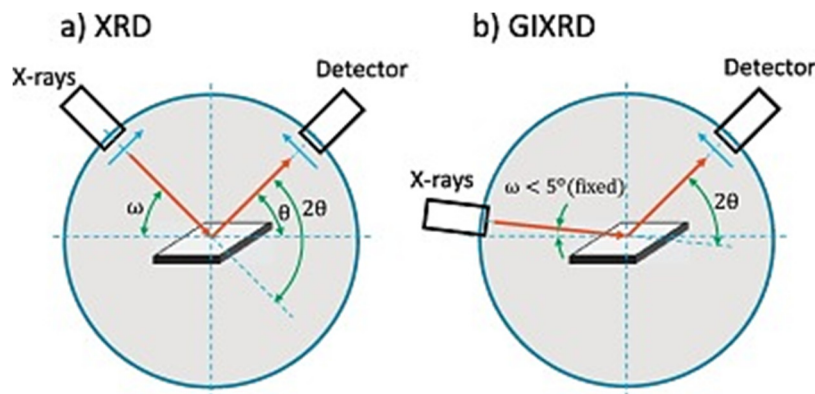
Figure 7: Schematic of: a) X-ray diffraction (XRD), b) grazing incidence X-ray diffraction (GI-XRD) technique geometries [62].

In a typical XRD technique, X-ray emitted from the X-ray source are reflected on the sample, and the angle between diffracted X-rays (θ) and the sample is the same ($\theta - 2\theta$), which is known as Bragg-Brentano configuration. In the GI-XRD geometry, a small incidence angle ($\omega < 5°$) is fixed while the detector is rotated around the sample [62]. The size of sub-micrometre particles or crystallites in XRD can be obtained by the Scherrer equation

$$\beta(2\theta) = \frac{k\lambda}{L\,Cos\theta} \qquad \text{Equation 2: Scherrer equation}$$

where K is a dimensionless shape factor, with a value close to unity. The shape factor has a typical value of about 0.9 but varies with the actual shape of the crystalline. θ is the Bragg angle, and β is the line broadening at half the maximum intensity (FWHM), after subtracting the instrumental line broadening, in radians. This quantity is also sometimes denoted as $\Delta(2\theta)$. Peak width (β) is inversely proportional to crystallite size (L or sometimes known as τ) [63].

The XRD measurements in this work have been carried out on a PANalytical X'Pert Pro MPD (Fig. 8). The crystal structure of the coatings deposited on Si-wafer substrates was analysed by the Cu Kα radiation ($\lambda = 0.179$ nm, k = 1.54 Å at 45 kV and 40 mA) through the scanning angle range of 5-90° (2θ) in grazing mode ($\omega = 2°$).

Figure 8: The XRD instrument used in this study.

3.2.3. AFM

Mainly the atoms exposed at the uppermost layers of the coating can be involved in tribological, mechanical and chemical reactions with the environment. Chen et al. demonstrated the removal of the single atomic layer due to the wear could be studied more accurately using AFM [41].

There are two main topography imaging modes, including contact mode and non-contact mode. In contact mode, the probing tip is in contact with the surface through a constant force of the cantilever. The force between the sample and the tip is directly proportional to the product of the displacement. However, the

contact mode hampers the health of the surface. In non-contact mode, the tip oscillates at its resonant frequency by an actuator. The decrease in displacement is measured as the probe is brought closer to the surface [64].

The oscillating mode/tapping mode of an AFM is an important subcategory of AFM image mode. As can be seen in Fig. 9, there is a cantilever with a very sharp tip to scan over a sample surface. The cantilever tip strikes the surface and moves up via oscillation in the vertical direction (z-direction). Simultaneously, the scanning rate in the x and y-axes is also tightly controlled.
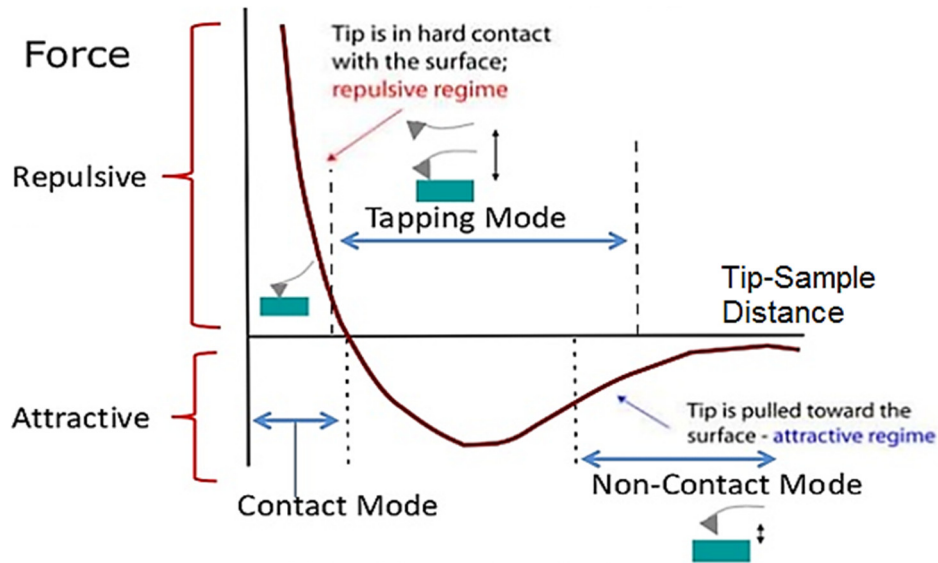

Figure 9: Modes of AFM operation, according to Lennard-Jones (LJ) potential [65].

The AFM machine in this experiment was model Vecco on a TMC vibration isolation desk, as it is shown in the following figure.

Figure 10: AFM instrument.

Setup values for AFM were adjusted according to the following data:

- Samples line: 512
- Scan rate: between 0.7 to 1 Hz
- Scan range: 5 micrometre
- The voltage of the laser: around 0.480

To acquire an image, the SPM raster-scans the probe over a small area of the sample, measuring the local property simultaneously. During this test, the specimen was moving under the tip. The adjacent of the laser on the tip is necessary for the first time, but it is not essential for others. Since the coating on the cantilever was an aluminium-based reflective layer for the first experiment, it had much higher voltage in the setup of the laser. The sample should be flat, without any dust, debris and fluid to capture true images. As silicon wafer is a very smooth substrate, it is a good candidate for AFM test. Due to the low hardness of the coating, the AFM test was conducted under a tapping mode. This mode provided images with higher resolution and without the tilt of the topology image. In this case, plane levelling is necessary for AFM process of the sample [66].

The AFM test provided four channels consisting of four data files, including a lateral signal and topography signal, both on forward and backward mode in the same line for each scan step. The data were analysed and visualised by Gwyddion software v. 2.53, which is a modular program for SPM data.

3.3. Nanoindentation

Nanoindentation technique has developed as an answer to the growing demands in the characterisation of small volumes of material. It plays an important role in probing the mechanical and functional properties of thin films [67]. This technique is a simple and fast method, probing a surface with unknown mechanical properties compared to the standard values. Nanoindentation is an indentation test as the development of the Brinell/Vickers hardness in Mohs hardness scale. It is the indirect measurement of the contact area, where modern nanoindentation instruments are very precise [68].

The length scale of the penetration in this technique is measured in nanometres. The Nanoindentation equipment usually included a Berkovich diamond pyramid indenter, a three-sided diamond pyramid with a half angle of 65.35°. Since the properties of the tip are known, the area of the indentation produced on the coating can be calculated from the penetration depth. This technique has become the predominant method for hardness measurement of thin films, which is the resistance of the material to plastic deformation [69]. Franz et al. this indenter can be used for Young's modulus measurements, in addition to hardness [70].

According to Stoney equation, the curvature of the film-substrate system, before and after deposition, relates to the induced stress during the deposition procedure. Therefore, the residual stresses of the film can be calculated in the nanoindentation test [68]. Fig. 11 shows a typical load-displacement curve of nanoindentation test.
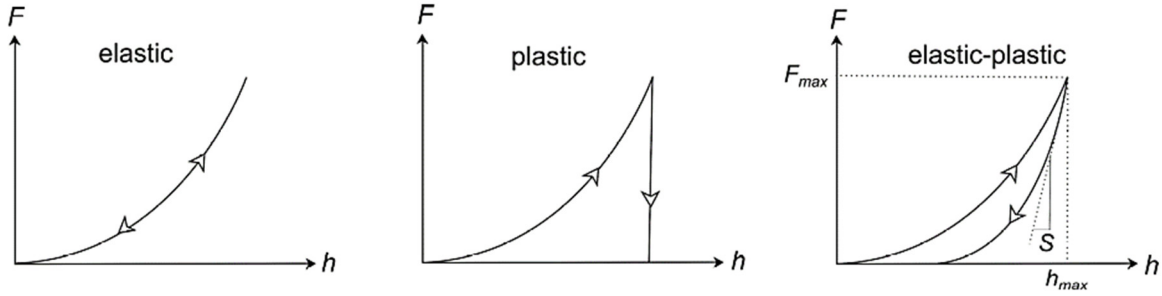
Figure 11: Typical representative load-displacement curves for nanoindentation [9].

Wide ranges of materials are deformed both plastically and elastically. A typical load-displacement curve represents a loading curve during deformation of materials, and an unloading curve as the elastic recovery area (Fig. 11). Based on these curves resulted from the nanoindentation tests, the measured hardness is calculated by dividing the maximum applied force during the indentation (F_{max}) by the projected area immediately before unloading (A_P)

$$H = \frac{F_{max}}{A_p}$$ Equation 3: Nanoindentation Hardness [71]

The measured hardness depends on the method of measurement. Nanoindentation is a technique for a very shallow depth of material, hence minimal influence from the substrate should be considered. In order to avoid substrate influence, the indentation depth should be controlled approximately maximum at 10% of the coating thickness [72]. The slope of the unloading curve can determine the stiffness of a material. For this purpose, the Young's (or elastic) modulus can be calculated using the Oliver and Pharr method [73]. The deposited films were analysed to determine their mechanical properties, hardness (H) and reduced elastic modulus (E_r), by nanoindentation tests (NanoTech Nanointerder - Micro-Materials Ltd.) equipped with a Berkovich diamond pyramid indenter (Fig. 12). During the test, a controlled pressure of a very hard tip into the coating applies a force to penetrate it on the coating. The resulting displacement is recorded to produce a force-displacement curve. The geometry of the indenter determines the size of the contact area [74].

The hardness values, used in this study were calculated from the average of 16 such measurements in two different locations on the coatings deposited on steel substrate (totally 32 different measurements for statistical purposes). The Oliver-Pharr method is used for the generation of the results. The measurements were performed on the free surface of each of the samples at ambient temperature (~24 °C) with 45 per cent humidity. The indentation depth was 7 to 10% of the coating thickness. In order to keep the hardness measurement independent of the substrate, the maximum applied a load of 3 mN was set. Figure A.1 in the Appendix includes the nanoindentation load-displacement curves. The loading/unloading rate was 0.17 mN/s, with a holding time at maximum load of 30 s to saturate creep effect before unloading.
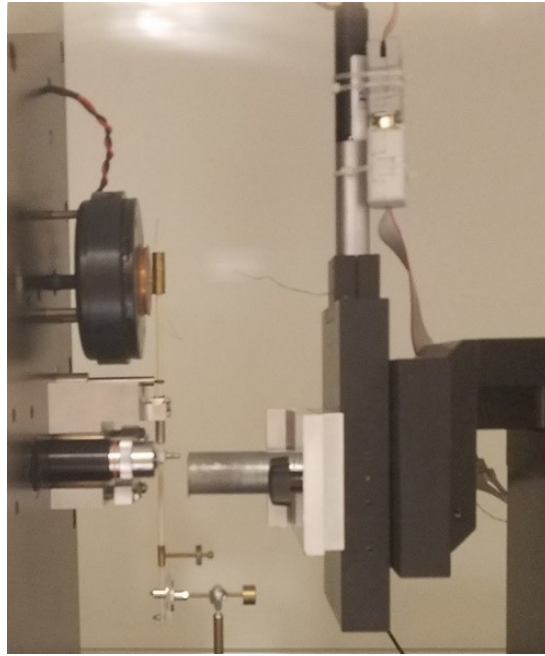
Figure 12: Nanoindentation equipment.

3.4. Adhesion Test

The adhesion/cohesion of the coating is an important factor for the tribological performance of the film. The adhesion, mainly evaluated by scratch test, allows determining how strong the coating adheres to the substrate. It can provide the critical load that is related to the adhesion properties of coatings. In this method, the load applied by a rounded diamond stylus normally pressed against a moving coated panel. While the load is increased gradually, the coating starts to fail at a certain value, producing torn edges with lifted coating along with the scratch. In the scratch test, there are two types of failures, adhesive that results in the delamination of the coating, this can present different ways of failure, extensive in the wear scar, or some parts. In addition, cohesive failures can be observed [75][76]. Fig. 13 represents the schematic diagram and the principle of the scratch test.
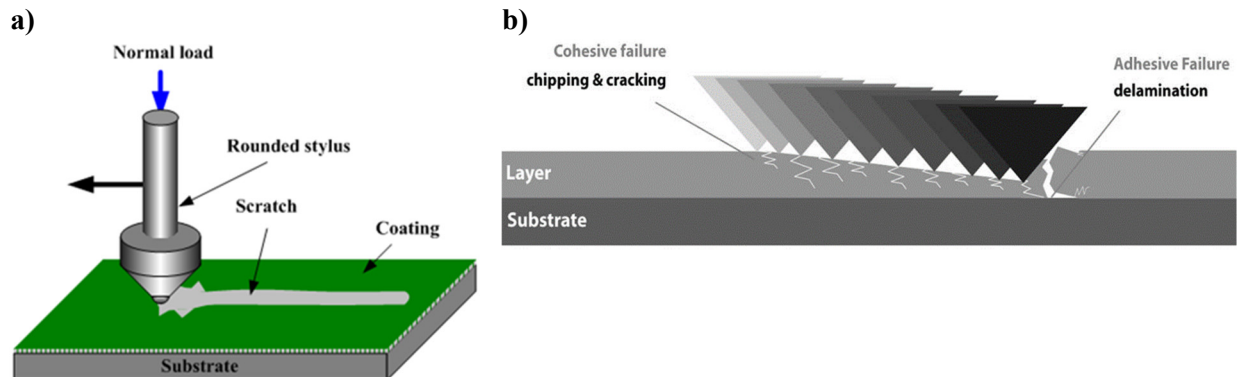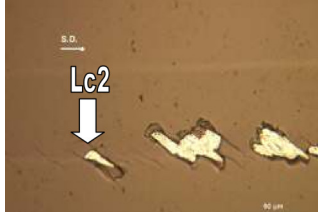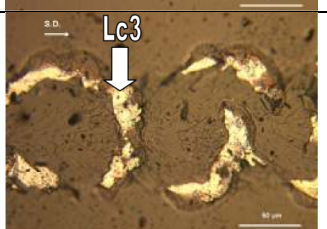
Figure 13: a) Schematic diagram of the scratch test instrument (not to scale), and b) principle of scratch testing [77].

The smallest load at which failure at the coating/substrate interface appears is known as the critical load (L_c), which is used to quantify the adhesive properties of the films. This value may be determined by examination of the scratch in a microscope [76][78].

The first incidence of the regular occurrence of the associated failure event will determine the value of L_C. There are three main L_C values, known as L_{C1}, L_{C2} and L_{C3}. The description of failure events and details of these values are summarised in Table 5.

Table 5: Classification of the critical load values in the adhesion test [79].

L_C	Description of failure events	Example Micrograph (SD: Scratch Direction)
L_{C1}	Forward chevron cracks at the borders of the scratch track. L_{c1} shall be taken at the closest end of the event to the scratch track start.	
L_{C2}	Forward chevron cracks at the borders of the scratch track, with local interfacial spallation or with gross interfacial spallation L_{c2} shall be taken at the failure event that occurs first, and at the closest end of the event to the scratch track start.	
L_{C3}	Gross interfacial shell-shaped spallation L_{c3} shall be taken at the first point where the substrate can be seen at the centre of the track in a crescent that goes completely through the track	

The panel used in the adhesion test should be a smooth and flat surface with uniform thickness. The main parameters of the test are the shape of the stylus tip, loading rate, stylus speed, and coating thickness [78]. The adhesion of the coating on the steel discs was evaluated using the scratch test apparatus, a Rockwell C conical diamond-shape indenter with a tip radius of 200 μm. The tests were performed on a CSEM REVETEST (model S/N – AOO 14-262) testing equipment. The adhesion tests were made using, a gradual increase of the load from 4 to 50 N at a rate of 100 N/min with a linear speed of 10 mm/min. According to ISO EN-1071-3, loading rate of 100 N/min, to generate a controlled scratch. The maximum load was limited to 50 N in order to prevent unnecessary wear of the stylus. At least two scratch tests were made on each coating. Optical microscopy is used to determine the critical loads regarding the standard for scratch test evaluation using a Leica DM4000 M LED microscope. This critical load can be used to quantify the adhesive properties of the coating. The optical images provided in an ImageJ software allowed calculating the adhesive critical load (L_C) at the time the film starts to fail. Fig. 14 shows the adhesion tester used in this work.
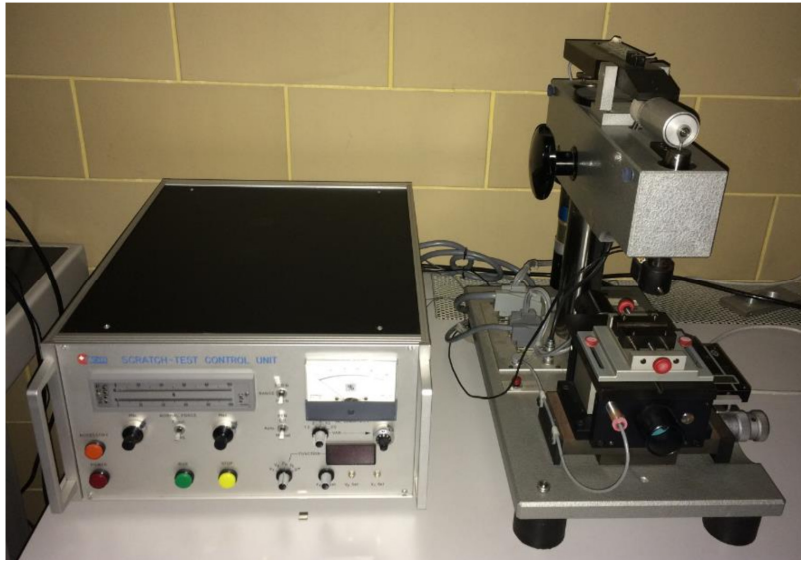
Figure 14: The scratch test equipment used for adhesion tests.

3.5. Tribological behaviour

Wear, as the key parameter of tribological behaviour of the surfaces, is the removal of material from its original position. In the case of sliding contacts, the quantification of wear is regularly in terms of the volume of material removed (V) and the specific wear rate (K') [80].

The tribological properties of the thin film in its desired application are complicated and expensive. Thus, it would be impossible to study the effect of individual real parameters. Model setups offer good early-stage development to study fundamental aspects of tribological behaviour of the coating using control of parameters such as contact geometry, load, and speed. Most widely used tribotesting geometric configurations are ball-on-flat and flat-on-flat [75].

One of the most versatile machines to study friction and wear properties of coatings and lubricants in a variety of sliding contacts is the SRV machine. SRV stands for German words "Schwingung, Reibung und Verschleiss", which means "oscillating, friction, and wear". For this tribological tester, genuinely manufactured components and standardised specimens can be used. Many lubricant producers and original equipment manufacturers (OEMs) use the SRV machine to evaluate the performance of their products, based on well-known standards such as ASTM, DIN, and ISO tests. For instance, it can be set up to run ASTM D5707-11, ASTM D7421-11, ASTM D7127-11, and DIN 51834. Among others, ASTM D5707 is similar to the well-known ASTM D4172 method for Four-Ball wear test. This method is used to measure the friction coefficient (μ) and wear that is run for a fixed time at a moderate load (Fig. 15) [81][82].
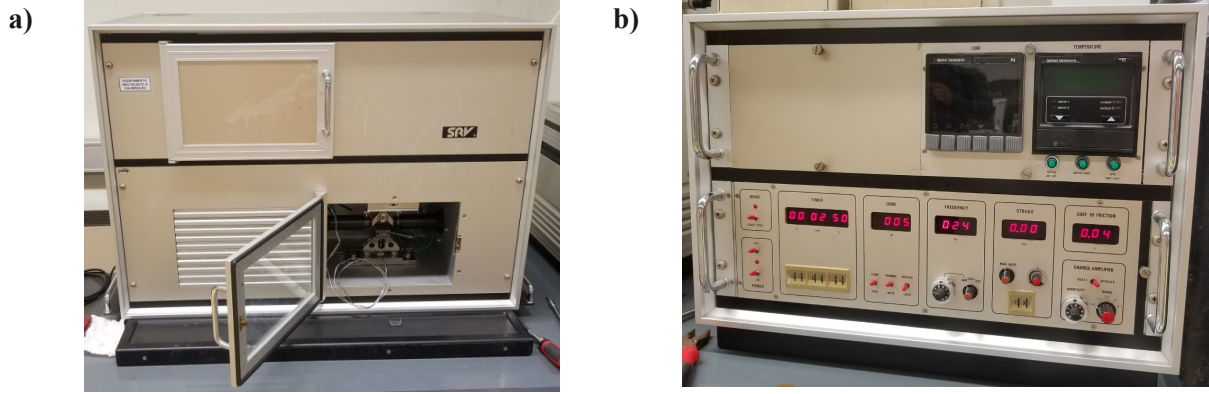
Figure 15: Standard SRV machine used for evaluation of the tribological behaviour of coatings; a) testing chamber, b) controller unit.

The SRV test can be conducted using many different specimens and configurations. Using ball on disc in a rotational or oscillational mode is particularly reported more than other configurations. If both upper and lower specimens are metallic, a computer can record the response voltage values proportional to the frictional force that imparted to the disc (lower specimen) during the test. The coefficient of friction (COF) can be calculated throughout the test using the relevant calibration curves. In the newer version of SRV machines, friction data can be recorded automatically by the machine controller. A non-metallic specimen, like various ceramic and plastics materials, can also be analysed in the SRV chamber. After testing, the wear scars can then be analysed using a 3D optical microscope to determine the volume loss and wear rate of each specimen, including the balls and discs [81][82].

The machine measures the mechanical interactions between two sliding surfaces in a loaded contact in either linear or rotational oscillatory motion. In the linear mode, which was used in this study, the upper ball (or pin) oscillates in a linear path on the lower stationary disc (Fig. 16). In this method, the controller unit can control the tribological parameters between the surfaces in contact [83].
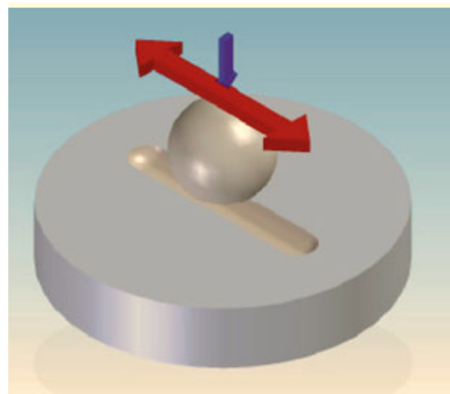
Figure 16: Schematic of ball-on-disc wear test setup in the SRV machine.

The SRV is a very adaptable instrument to simulate specific needs best. General tribological experiments and test variables of this machine are summarised in the following table:

25

Table 6: General tribological tests properties and technical variables of SRV test.

Tribological tests properties	Technical variables
Assessment of wear resistance	Load: 5 - 2000 N
Possibility to perform dry and lubricated tests	Frequency: 1 - 500 Hz
Possibility to use reducing or oxidising atmosphere	Stroke length: 0.1 - 4 mm
Controlled by the geometry of specimens	Different type of contact
Possibility to conduct high-temperature tests	Temperature: RT - 900 °C

For determination scars volumes, and consequently, the volume of material removed and wear rates, the horizontal and vertical length of wear scars should be analysed under an optical microscope, and then measuring the sectional area removed. Consequently, wear volume is calculated using Equation 4

$$V = \frac{\pi . d_{sr}^4}{64.R}$$ Equation 4: Wear volume for balls

Where R is the radius of the sliding ball (upper specimen in the SRV machine) and d_{sr} is the average of the horizontal and vertical length of wear scars on the ball according to Fig. 17 and Equation 5

$$d_{sr} = \frac{d_1 + d_2}{2}$$ Equation 5: Average length of wear scars on the ball
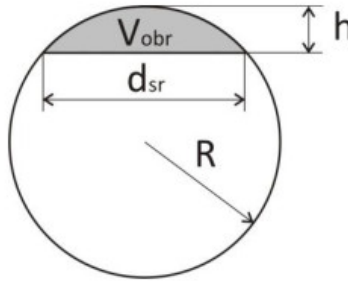
Figure 17: Wear geometrical scar values for the sliding ball [2].

For the discs, V can be calculated by Equation 6

$$V = A_{Avg} * L_s$$ Equation 6: Wear volume of discs

where A_{avg} is the average area of the wear track, and L_s is the stroke length. Accordingly, wear rate for both specimens can be determined through the following equation

$$K' = \frac{V}{S.F_N} \ [mm^3/Nm]$$ Equation 7: Wear rate

26

where F_N is the applied normal load (N) and S is a total running distance of the ball over the disc or the sliding distance (m), the result of multiplication of test time, t, and sliding speed, v

$$S = t.v$$ Equation 8: Total running distance of the ball over the disc

The unit of V and K' are m^3 and m^2/N, respectively, but the volume loss and wear rate are mainly reported as mm^3 and mm^3/Nm, respectively [2].

In this study, the configuration of the test rig was a ball-on-disc similar to Fig. 18. For this purpose, flat steel discs with three different WSCF coatings run against a counter ball-shape surface. The sputtered thin films were evaluated initially at room temperature and further at an increasing temperature in order to record the variation of friction coefficient continuously. The same procedure was done under dry and lubricated conditions.
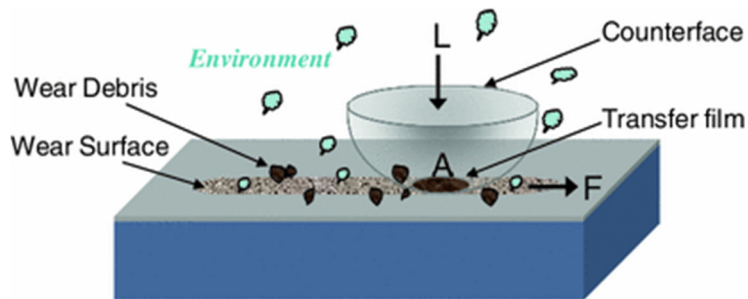
Figure 18: Schematic of a hemispherical ball sliding on a solid lubricant-coated sample. Wear surface in contact with the transfer film on the counterface ball [6].

In favour of studying the tribological performance of the sputtered film under dry and lubricated conditions, tests were conducted at dry (0 %Rh using N_2 gas flow) and wet (35 %Rh of natural air) conditions. The influence of temperature on the coatings was investigated at two different temperatures of 25 °C (RT), and 200 °C (HT) exposed to natural air. The elevated temperature corresponds to most of the applications where these coatings can be used. Conditions of the tribological testing are summarised in Table 7.

Table 7: Tribological testing conditions.

Testing condition	Description
Air-RT	Coatings were exposed to 35 %Rh of natural air at room temperature (25 °C)
Air-HT	Coatings were exposed to 35 %Rh of natural air at high temperature (200 °C)
N_2-RT	Coatings were exposed to 0 %Rh using N_2 gas flow at room temperature (25 °C)

In order to ensure repeatability of results, three measurements were taken for each coating. The average of three measurements made on three different balls and related zones of the wear track on discs. WSCF coated discs were tested in SRV-OPTIMOL reciprocating testing equipment using 100Cr6 steel balls (diameter 10 mm) as upper sliding specimens. The SRV tests were conducted at a constant vertical load (5 N), frequency (25 Hz), test duration (600 s, 15000 cycles for 60 m sliding distance), and stroke length (2 mm). Different testing environments were used, including different temperature (RT and HT) and humidity (35 %Rh Air and dry nitrogen). Fig. 19 illustrates inside the SRV test chamber used for studying the tribological behaviour of the coatings. The setup of the heating apparatus was controlled by a thermocouple to maintain the substrate surface temperature as close to the desired temperature as possible.
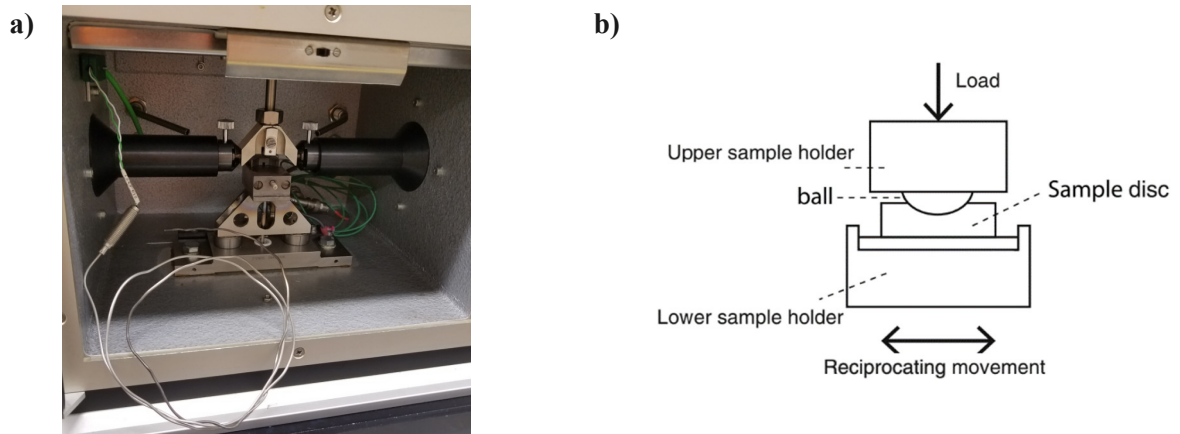
Figure 19: a) Inside the SRV chamber, and b) schematic of a sample arrangement in the test chamber.

The surface coating topography and the wear track of balls and discs were analysed by a 3D optical profilometer, Alicona InfiniteFocus, Alicona Imaging GmbH (Fig. 20). It is used for determination scars volumes, and consequently volume loss and wear rates.
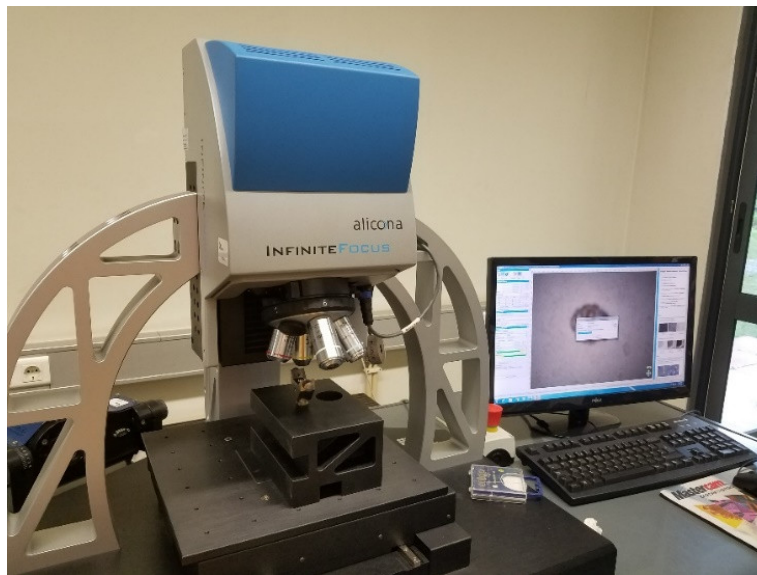
Figure 20: The 3D optical profilometer used in the current work.

In addition, an optical microscope manufactured by Leica Microsystems CMS GmbH (Model No.: DM4000 M LED) is used to capture the images of full wear track on the discs in the magnification of 20X.

Chapter 4 - **Results and discussion**

4.1. Structural characterisation

4.1.1. SEM/WDS

Both top view and cross-section SEM images of coatings presented in Fig. 21&22 were captured at the magnification of 25 KX.

(a)   (b)   (c)

Figure 21: SEM characterization of the top surface of (a) WSCF1, (b) WSCF2 and (c) WSCF3 (scale bar: 200 nm).

(a)   (b)   (c)

Figure 22: Cross-sectional SEM image of (a) WSCF1, (b) WSCF2 and (c) WSCF3 (scale bar: 200 nm).

An overview of the coating surface with quite compact structures can be seen from these images. As the coating has been prepared by sputtering, the presence of droplets on the surface coatings is because of arc discharge during the deposition procedure. From the SEM images, it can be seen the morphology of the films is the typical cauliflower-like structure.
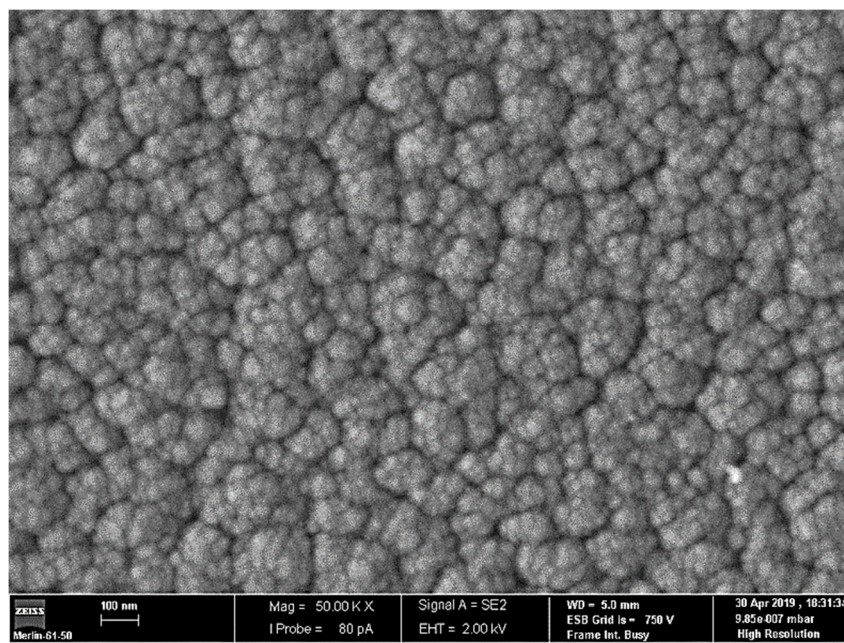
Figure 23: SEM top view of WSCF3 at higher magnification (50 KX).

As we can see from the overall surface, WSCF3 and WSCF2 have more homogeneous structures than WSCF1. For a higher amount of carbon in the structure, the coatings become denser. In addition, fissures and agglomeration could be detected on the surface of WSCF1 (Fig. 21.a).

The SEM images of the cross-section of the sample clearly show two different layers of the coatings on the substrate, including Cr interlayer as the first layer, and the coating in the top layer. They represent columnar morphology for the coatings, which is characteristic of sputtering techniques, where new material is continuously deposited on the previously deposited layers of the WS_2-based thin films [42][84].

The cross-section view allows us to see the thickness of the coating and interlayer. It can be seen that the thickness of the coatings for WSCF1, WSCF2 and WSCF3 is roughly 1.702, 1.715 and 1.911 μm, including the chromium interlayer thickness of 0.272, 0.277 and 0.304 μm, respectively. The change in the morphology of the coating with the addition of C alloying element and F dopant confirmed by SEM images. The morphology of coatings was according to Nossa's works [40][85]. It has been observed for the WS_2-based coatings; the morphology is usually columnar for carbon contents lower than 30 at.% [86].

As-deposited pure WS_2 coatings have a porous and columnar structure, with very distinct flakes in some cases. The appearance of these coatings is usually velvet to black and velvet-like. Because of poor adhesion of the standing flakes, they can be easily scratched [85].

In comparison, a higher amount of carbon and fluorine (Fig. 22) increased the thickness in the cross-section of coatings and the corresponding interlayers, such that WSCF3 coating was thicker and denser than others

were. In WSCF1, fissures are detectable from two-third upper thickness until the surface, and the film porosity largely increased in the top layer (Fig. 22.a). In other words, the increase of the alloying element contents resulted in a featureless morphology with a lower level of porosity and higher compactness. In particular, increasing C contents indicates the improvement of the morphology of films.

Table 8 represents the WDS results for the coatings and their total thickness obtained by SEM. The film first deposited without applied power on C cathodes for WSCF1. The presence of C is because of CF_4 partial pressure in the deposition chamber. The chemical composition of WSCF2 and WSCF3 coatings indicates that higher applied power on C cathodes increases the carbon contents in the film, while W and S are decreased. With the increase of the power on the C targets, there was a linear increase of the C content. However, there was not a direct correlation between increasing C contents and the amount of F in the film as that WSCF2 had the lowest O, highest F and middle-range C contents. It means there was no direct relationship between increasing C contents and the concentration of F in the coatings. As it is shown in Table 8, the ratio of alloying elements over the main elements ((C+F)/(W+S)) was increased from 0.19 to 0.34 and 0.39 for WSCF1, WSCF2 and WSCF3, respectively. Therefore, it can be concluded from SEM and WDS results, increasing alloying elements in the samples enhanced the compactness of coatings by decreasing the number of porosities and the thickness by increasing alloying elements.

Table 8: The chemical composition and thickness of the coatings.

Sample	Chemical composition (at. %)						S/W ratio (–)	F/C ratio (–)	(C+F)/(W+S) ratio (–)	Thickness (µm)
	W	S	C	F	O	Cr				
WSCF1	29.5	50.2	10.4	5.3	4.5	0.5	1.7	0.5	0.19	1.70
WSCF2	27.9	44.3	15.5	9.3	2.6	0.4	1.6	0.6	0.34	1.71
WSCF3	25.8	43.9	18.7	8.5	2.7	0.4	1.7	0.5	0.39	1.91

The S/W ratios align well with the values of previous studies. Mutafov et al. [35] reported that during ion bombardment of the cathodes, the element with lower atomic mass (S) is more likely to be ejected from the substrate than the heavier one (W) [42].

Since WSCF1 was less compacted than the other two samples with a higher amount of alloying elements, it is more likely adsorbed contaminants like oxygen. The oxygen presence in the sputtered coatings can be considered as normal regarding the deposition methods and the types of deposit. It may be originated from the residual water vapour in the deposition chamber [35][87].

Although the detected concentration of O can reach values greater than 10 at. % [88], its contents in this work were lower than 4.5 at.% and not higher than in dopants in the coatings.

Generally, the concentration of oxygen in the coating conversely depends on the deposition rates, i.e. higher rates will decrease the contamination O. With the increase of the power on the C targets, there was an increase of the deposition rate. In order to make ensure the contaminants were independent of the processing time, the deposition time should be kept constant [89].

4.1.2. XRD

XRD results of the coatings are shown in Fig. 24. As we can see, there are four characteristic peaks of the hexagonal WS_2 for all coatings located at $2\theta \approx 14°$, $34°$, $60°$ and $70°$, which can be assigned to the (0 0 2), (1 0 0), (1 1 0) and (1 0 8) planes, respectively [42][87]. These peaks are in agreement with the ICDD card no. 00-002-0131 and literature results [90].

The two peaks, indexed as Si (3 1 1) and Cr (1 1 0), corresponding to the substrate and interlayer, respectively. Regula et al. showed that the broad area around the low-intensity peak (0 0 2) indexed at $2\theta \approx 14°$ corresponds to the beginning of the formation of the basal plane of WS_x thin films parallel to the substrate surface [87]. The sputtered sample with low carbon, and fluorine content (WSCF1) shows the classic diffraction patterns of WS_x-based TMDs with asymmetrical peaks at $2\theta \approx 34°$ indexed as (1 0 0) planes. There is an extended shoulder for higher angles ($2\theta \approx 34°$ to $44°$) of each sample corresponding to a feature of a phenomenon called turbostratic stacking of S-W-S single layers [87].

These sandwich layers in WS_2 are the family of (10L) planes (L: 1, 2, 3). The weak interactions between two layers cause rotational and/or translational disorder around the c axis, relative to each other. Along with two more peaks at $2\theta \approx 60°$ and $70°$, respectively assigned to the (1 1 0) and (1 0 8) planes, this XRD pattern is typical of WS_x films [91][92].
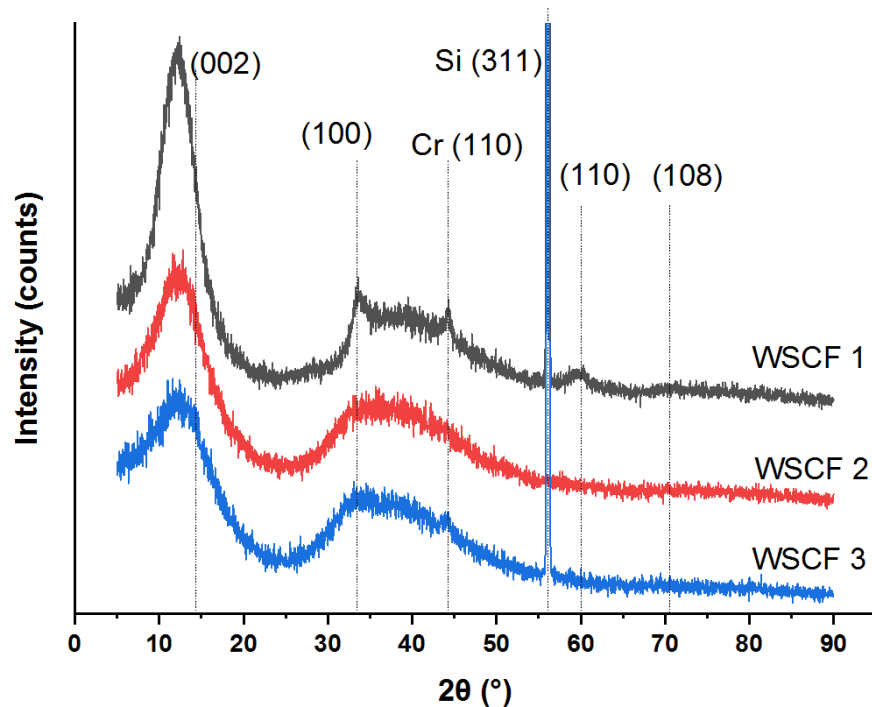
Figure 24: XRD diffractograms of WSCF coatings deposited on Si-wafers.

Depending on the alloying content, different peak positions, intensities and broadening were observed. Amorphous materials do not have a periodic array with long-range atomic order and therefore produces only broad scattering features. Therefore, the diffraction from them does not show sharp Bragg peaks [93]. As it is shown in Fig. 24, only WSCF1 (with the lowest alloying content) presented obvious crystalline peaks related to the WS_2 structure. In comparison, increasing fluorine and carbon content in the films

gradually decreased the crystallinity. The less intense and broader peaks in the XRD patterns of WSCF2 and WSCF3 coatings suggest amorphous coatings. Thus, the coating becomes amorphous for a C and F contents of over 15.5 and 9.3 at. %, respectively. Increasing alloying contents (C and F) lead to a big change in the preferential orientation of the thin films, with (0 0 2) reflection prevailing over all the others [35]. In addition, the fluorine incorporation contributed to a smooth shift of the (0 0 0 2) basal plane position toward the left side (lower angles). Because the hexagonal structure is expanded by insertion of the fluorine on the WS_2 lattice leading to the d-spacing which increase of adjacent WS_2 sheets resulting in a reduction of the van der Waals bonding energy [42].

The XRD observations were by the alloying ratio ((C+F)/(W+S)) determined by WDS study and images of SEM cross-sections. According to literature, the crystalline WS_x coatings with distinctive peaks in their XRD patterns were reported to be porous and flaky. While dense and featureless microstructure and morphology were related to amorphous TMDs with broad XRD spectra. Based on SEM images, the same condition rules the coatings in the current study [9][42].

Increasing diffusivity of the alloying atoms in the WSCF coatings may explain the difference in crystallinity between pure and alloyed WS_x TMDs. According to Nossa et al., WS_x TMDs present the WS_2 hexagonal phase, which is preferentially oriented after (1 0 0) plane [94].

Zabinski et al. showed that the fluorine incorporation led to either an expansion of the d-spacing in basal direction or an increasing disorder of the WS_2 structure in the WSCF coatings deposited by PLD method [15]. Based on the Mutafov et al., the size of the (0 0 2) oriented crystallites for the sputtered WS_2 films (~ 3 nm), is lower than those with the (1 0 0) plane parallel to the surface (~6 nm) [35].

Rodrigues et al. indicated that the (0 0 2) peak at 2θ≈14° for WSCF films, slightly shifted to lower angles compared to pure WS_2 coatings, suggesting that fluorine should be incorporated in the WS_2 phase. They also showed the presence of W-C bond using X-ray photoelectron spectroscopy (XPS), however, WC grains should be very small, which XRD could not detect them [42]. In another study, Voevodin et al. reported WC nanocrystallites were observed in TEM but not in XRD. Therefore, it seems the alloying phases being present in the films formed amorphous W-C-F -contained grains, and thus consist of small clusters with limited long-range order [39].

4.1.3. AFM

The results of the AFM test for samples are shown in Fig. 25. Since the samples in tapping mode had a height range in the same values for the forward and backward scan, the forward images were selected to represent here. The 3D topology images are also shown next to the related 2D images. The effect of adhesion can determine through subtracting backward result and the forward result, which can eliminate the influence of roughness. It means, the difference in topography is due to the bending in the cantilever as a result of adhesive force between the tip and the surface of the second sample. Accordingly, a comparison of forward and backward scanning direction gives an accurate image of the surface and its adhesive properties [95].
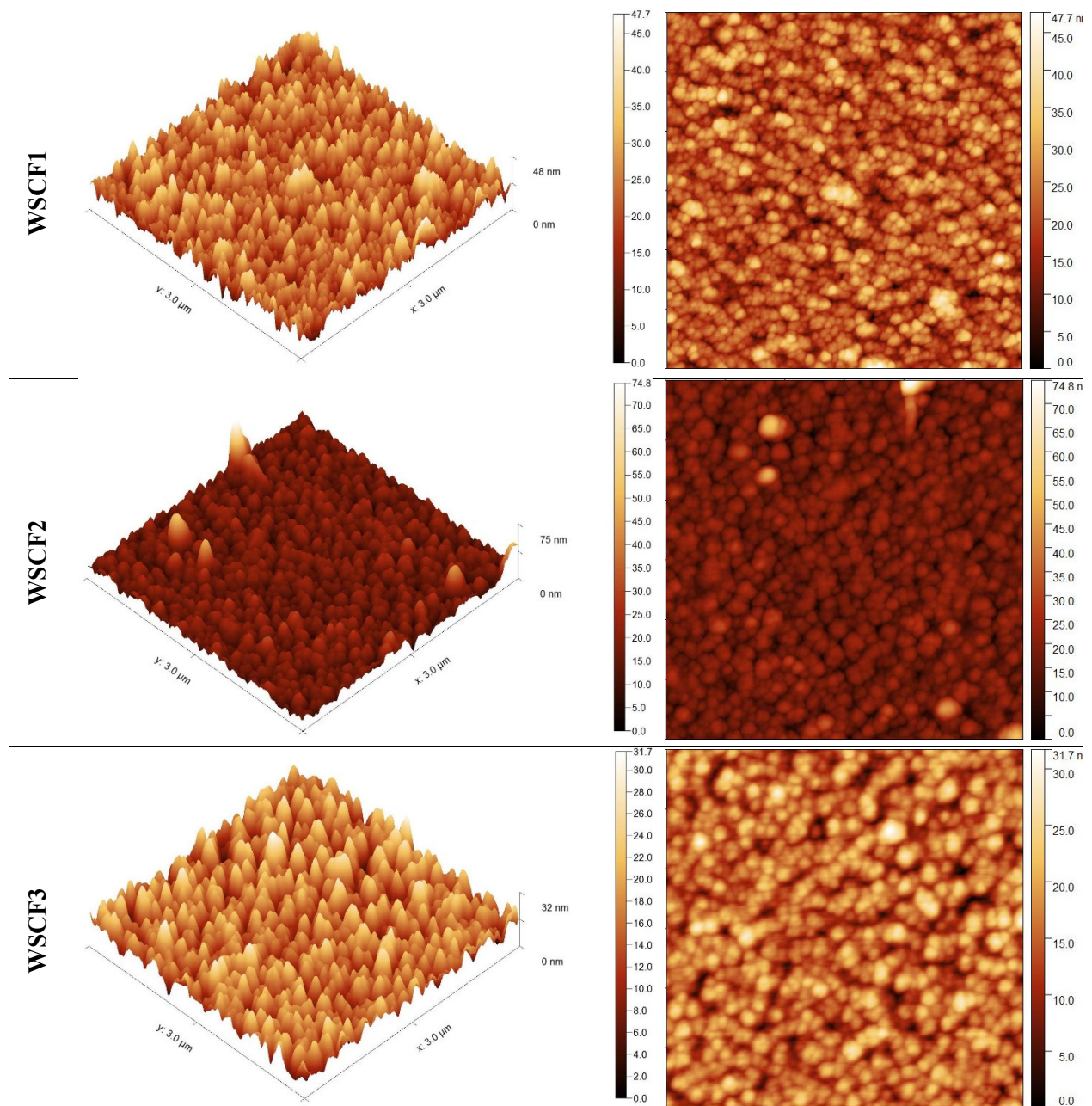
Figure 25: 3D (left) and 2D (right) AFM topographical images of coatings.

The same behaviour in height ranges of backward and forward images confirms the presence of adhesive force is neglectable. As it can be seen from the 3D AFM images, the morphology of the coating is cauliflower with lots of small rounds–shape structures on the surface. The morphologies based on AFM results are in good agreement with the structural observations from SEM images. In Fig. 25, we can see there is some irregularity in peak distribution on the surface of WSCF2 sample, which affects the maximum value of the height scale. However, regarding the surface roughness and morphology of two samples, data in Table 9 indicates RMS roughness (Sq) and Mean roughness (Sa) for sample WSCF1 is higher than WSCF2, while WSCF3 has the lowest values of roughness parameters. In another word, the highest amount of carbon in the coating led to much smoother surfaces.

Table 9: Surface roughness of WSCF coatings.

Parameter	WSCF1	WSCF2	WSCF3
RMS roughness (S_q) - nm	5.9	5.1	4.2
Mean roughness (S_a) - nm	4.7	3.5	3.4

4.2. Mechanical evaluation

4.2.1. Nanoindentation

The elastic modulus and hardness (Fig. 26) of coatings are slightly different, but these values characterise the average properties of the surface films. The calculated results are shown in Table 10. Both Young's modulus and hardness of WSCF1 are higher than those of WSCF3. The WSCF2 showed the lowest hardness; however, this coating represented the highest reduced Young's modulus. It suggests that the F incorporation in the structure did not change the hardness significantly, and the Reduced Young's modulus were almost the same for the studied WS_x-based coatings.

Table 10: Hardness and Reduced Young's modulus of coatings.

Coating	Hardness [GPa]	Hardness error [GPa]	Reduced Young's modulus [GPa]	Reduced modulus error [GPa]
WSCF1	3.72	0.16	61.97	0.92
WSCF2	3.57	0.09	62.51	1.81
WSCF3	3.65	0.17	59.36	1.33
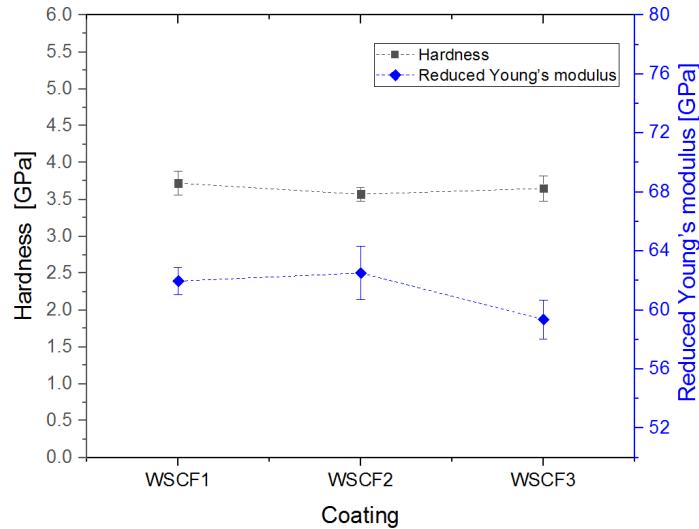
Figure 26: Hardness and reduced Young's modulus of WSCF coatings as a function of carbon content.

4.2.2. Adhesion

Optical micrographs of the scratch tracks are shown in Fig. 27. The images represent the failure characteristics of WSCF coatings on M2 steel. The left images show the completely scratch track, while the right images represent a double magnification of the end part of the track for better comprehension of the test.
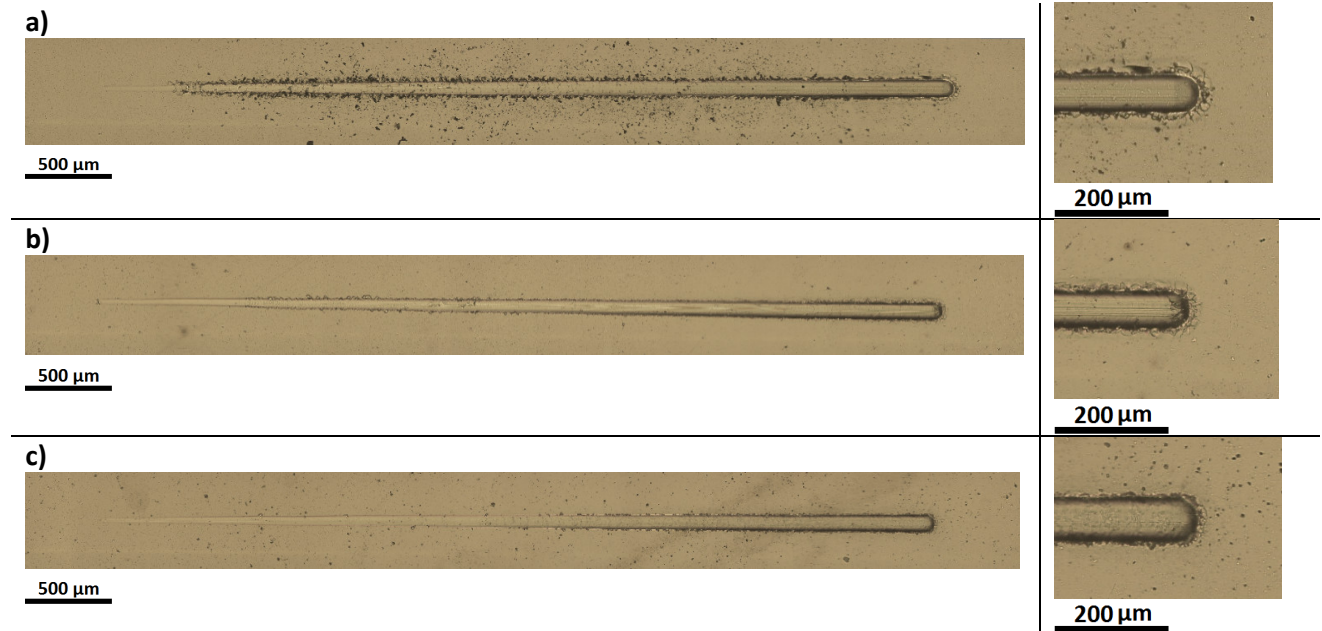
Figure 27: Optical images of the scratch traces of (a) WSCF1, (b) WSCF2 and (c) WSCF3 obtained from the scratch test (10x magnification). The right images are the final part of the scratch test (20x magnification)

For coatings in as-deposited conditions, the quantitative results of the scratch tests are given in Table 11. L_{C2} is the first adhesive chipping at track edges, and L_{C3} corresponds to initial failure determined by scratch testing. Although critical load values of first adhesive chipping were relatively low, all coatings could show good resistance to failure until the end of the test (50N). Even for the highest applied loads, the appearance of the scratches was rather promising, and there were no extensive delaminated zones close to the track.

Table 11: Failure load values of WSCF coatings.

Coating	Failure modes [N]	
	L_{C2}	L_{C3}
WSCF1	8	>50
WSCF2	13	>50
WSCF3	25	>50

As shown in Table 11, no similar trend to the hardness could be observed for the adhesion. While the addition of F does not have a linear effect on the L_{C2} values, more carbon in the coating increases the failure load values. According to the cross-sectional SEM images of coatings (Fig. 22), the thickness of the

coatings for WSCF1, WSCF2 and WSCF3 were roughly 1.702, 1.715 and 1.911 μm, including the chromium interlayer thickness of 0.272, 0.277 and 0.304 μm, respectively. Therefore, this agreement between L_{C2} values and the C content in the coating should be related with the composition and more compactness of WSCF3 coating compared to the others, suggesting that the higher alloying elements and more compactness improved the adhesion behaviour of this coating.

4.3. Tribological behaviour

Since this study is aimed at investigation of the tribological properties of low-friction WSCF coatings, thus its relation to the morphology of the sputtered films should be considered in order to discuss the role of alloying elements (C and F) in these solid lubricant coatings. More specifically, the main goal is to develop and understanding of such coatings at varied conditions, including different temperature and humidity. Accordingly, three different sets of coatings, based on WSCF, were tested to determine the COF. The ball-on-disc tests were performed on the WSCF coatings during the 10 minutes or 15000 (15k) sliding cycles. Results were obtained at room temperature and 200 °C exposed to the natural air, as well as dry condition exposed to N_2 flow at room temperature. The resulting COF versus sliding time obtained from the friction tests performed are displayed in Fig. 28.
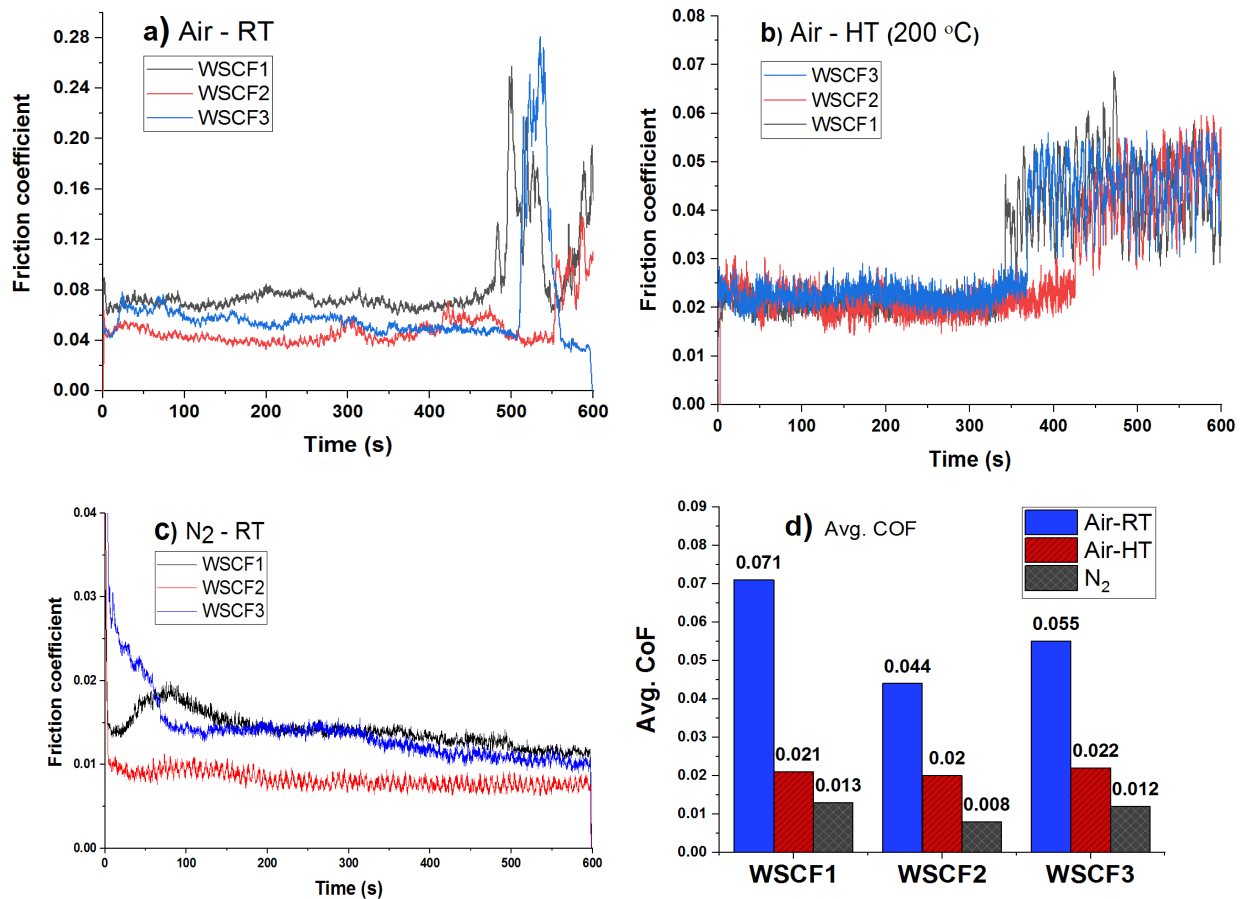

Figure 28: The mean coefficient of friction of WSCF coatings tested at: (a) air at 25 °C, b) air at 200 °C, (c) dry N_2 gas flow at 25 °C, and d) relative comparison of average COF for the deposited coatings.

As can be seen from Fig. 28, all WSCF coatings tested for 600 s presented the average COF in the range from 0.008 to 0.071. These values confirm that WSCF coatings maintain low COF despite almost complete removal of the coating material, in agreement with the literature. The general trend of decrease in friction coefficient with increasing the alloying elements is attributed to the theory, that more C and F in the coating can ease the crystalline slipping of the basal planes that are weakly bonded to each other with the van der Waals force [42].

Generally, the tribological behaviour of WS_x-based coatings depends on the nature of the coating material, contact geometry, applied load (the contact pressure), and the environment. The friction coefficient is lower for higher normal forces [96]. Despite the significant difference in the COF trends, the obtained values of the coefficient of friction indicate the overall solid-lubrication behaviour for every sample at each condition is likely similar together. The average COF for Air-RT, Air-HT and N_2 can be measured in the steady-state between 30 to 480 s, 30 to 350 s and 150 to 600 s, respectively. While the failures in the coatings happened after 470 s at the Air-RT and 340 s at the Air-HT condition, whereas no coatings failed at the dry N_2 atmosphere. It means the lubrication performance of the thin films remained in the best condition in the dry environment. In contrast, the aggressive condition of Air-HT environment led to a faster failure compared to the Air-RT and N_2 for all three coatings because of the coatings removal or partial removal at the contact area with the ball counterpart.

An effect of chemical or structural changes of the materials on surface results in the formation of tribolayers or tribofilms in the contact. Before the steady-state area, there is an unstable short period showing some fluctuations in the COF values. It could be related to the gradual formation of a tribolayer on the counterpart surface during the running-in period [97].

Therefore, the presence of steady-state region in the COF diagrams could be possibly due to the formation of these layers. Low-shear strength tribofilms in dry condition or vacuum air atmospheres result in extremely low friction coefficients because of the inert basal planes and lamellar structure existing in the individual crystallites of TMD films [98].

It seems the formation of a (0 0 0 2) well-oriented WS_2 tribo-films is responsible for the low-friction mechanism of the prepared WSCF coatings. The variation in COF values indicates that the formation and destruction of a low friction layer are occurring. The understanding and control of the behaviour of these layers are important for tribological optimisation [99].

A further decrease in the friction coefficient after 200, 250 and 300 s for WSCF1, WSCF2 and WSCF3, respectively, is due to the reorientation process in some parts of the wear track by fresh material from the coating. From the failure area of the RT sliding test (approximately from 480 to 600 s), a consequent strong increase of coefficient friction in a very irregular way avoids the reformation of tribolayers. Moreover, the progressive attachment of oxides to the wear track is another cause of increasing COF values.

The measured COF could be the friction between the sliding WSCF coating and the part of the transfer layer because of partial removal of the thin film. Thus, it is expected that materials of WSCF coatings are worn and then adhere to the top layer in the contact forming tribo-transfer layer. The measurement of the same coatings during longer and shorter SRV tests demonstrated a similar trend in the COF values.

In all conditions, the evaluated WSCF2 coating exhibited the lowest and most stable friction behaviour. As we can see from Fig. 28.d, WSCF2 showed the lowest COF values of 0.044, 0.020 and 0.008 at Air-RT, Air-HT and N_2, respectively. In other words, WSCF2 had the optimum coating composition among the sputtered films regarding the solid lubricity.

The COF curve of WSCF2 film at dry condition is a very smooth and approximately constant low value (COF=0.008) along with the entire test. This coating is much denser than other samples, and it presented the lowest hardness and highest reduced Young's modulus based on nanoindentation tests, which can explain the low and the constant value of COF for this sample. Concerning the surface roughness of WSCF coatings, AFM results indicated that WSCF3 had the smoothest surface. Since after the running-in period the effect of the roughness is removed, and it will not influence the friction, weaker van der Waals bond between the inter and intra-crystalline slippery layers in the TMD structure had the main effect on the low COF for WSCF2.

XRD patterns can explain why the calculated friction from tribological tests for WSCF2 (the highest amount of F) was lower than WSCF3 and WSCF3 at both room temperature (%Rh of 35%) and 200 °C (dry) conditions. The weaker van der Waals bonds in the surface are due to more fluorine incorporation in the S-W-S layers. Furthermore, the F can prevent WS_2 oxidation by withdrawing more electron density than oxygen attaching to high energy sites in the W_z non-bonding orbital, which result in the easy shear ability of the tribofilm. As it was presented by the shift in the (0 0 2) XRD peak, the presence of F in the structure also leads to the expansion of the WS_2 network in the basal direction. This phenomenon is like the sulphur substitution by oxygen in the MoS_2 matrix [15][100].

Although WSCF1 showed the highest value of COE at Air-RT (0.071) and N_2 (0.013) compared to the WSCF3 Air-RT (0.055) and N_2 (0.012), it presented lower COF of 0.021 in comparison with 0.022 at Air-HT condition. It suggests a high amount of alloying elements in the structure can increase the friction force at elevated temperature, possibly through accelerating the oxidation by a high amount of carbon. This behaviour is in contrast with the general decreasing trend for COF values for higher alloying ratio ((C+F)/(W+S)) in the WSCF coatings.

All WSCF sputtered films tested at high temperature (Air-HT) have the friction coefficient lower than that of obtained at room temperature. Regarding the effect of elevated temperature on the friction force on the contact surface of WSCF coatings and steel ball, Polcar et al. proposed that higher temperature facilitates the intercrystalline slipping of hexagonal WS_2 structure as a transferable tribolayer in the contact area [84]. Higher COF at Air-RT condition is because of the oxidation of the dangling bonds in the S-W-S layers. Accordingly, the presence of humidity increases the interplanar bonding energy, creating abundant wear debris that can adhere to the counterpart ball, as the shearing forces can easily destruct the soft tribofilm in the contact surface. Rodrigues et al. reported that these wear debris are not oxidised in the presence of humidity when flaking from the coating [42].

WSCF coatings represent the typical behaviour of WS_x thin films when tested in humidity-containing air atmospheres. In particular, WSCF1 follows a COF decrease in the early stage of the test, due to the alignment of WS_x basal planes in the sliding contact. Besides, the time necessary for the formation of the tribolayer in the running period. Subsequently, strong instabilities are then observed related to the destruction and reformation of the low friction tribolayer [99][101].

Surface profilometry of the wear tracks was performed in order to understand the tribological behaviour of tested materials. Obtained results were used to calculate the coatings volume loss and wear rates. Fig. 29&30 provide a better idea of the tribological performance of the coatings after SRV test.

	WSCF1	WSCF2	WSCF3
Air-RT			
Air-HT			
N₂			
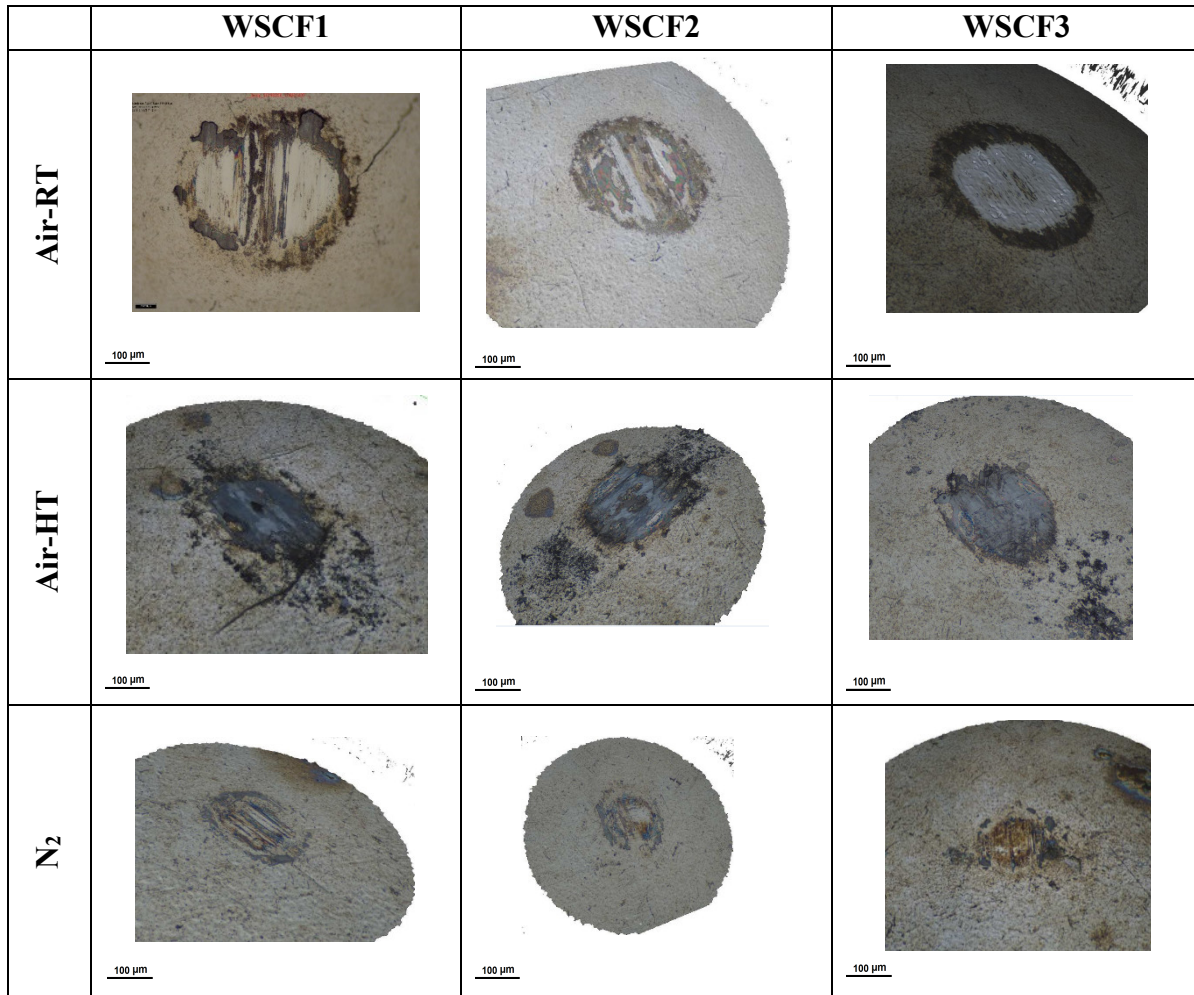
Figure 29: Optical microscope micrographs of ball scars after the SRV wear test (scale bar: 100 µm).

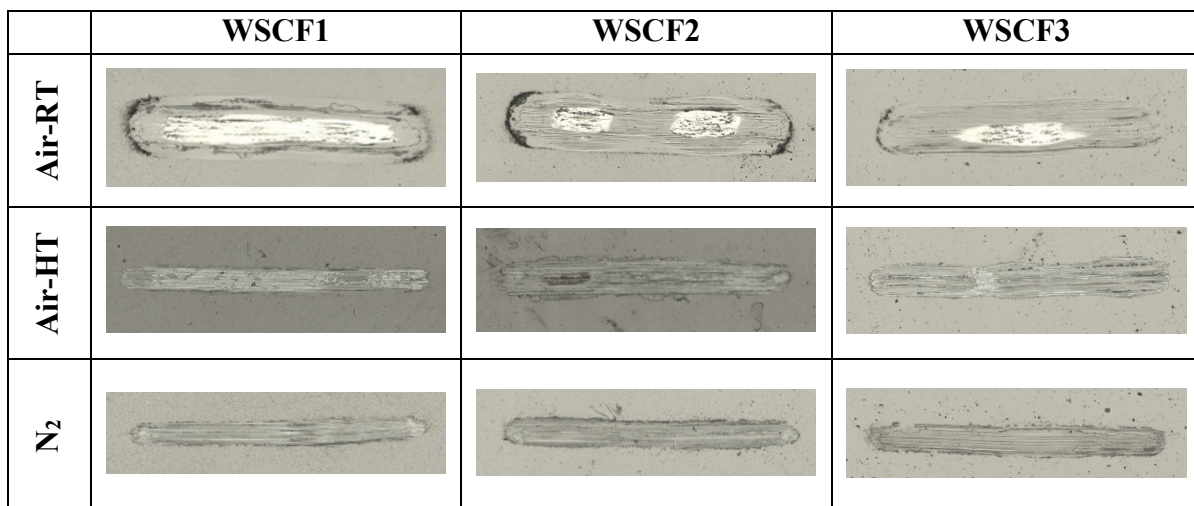|	WSCF1	WSCF2	WSCF3
Air-RT			
Air-HT			
N₂			

Figure 30: Optical microscope images (20X) of wear scar (length: ~2 mm) on the WSCF sputtered discs after 15000 cycles of SRV tribological test.

As it can be seen in the micrographs of the balls, wear scars almost are in round-shape, and they are covered by adhering transfer films. In more details, the images reveal that small islands of adhering material are present on the surface, instead of a stable transfer film. It seems the difference among the appearance of the wear scars is related to the change in the physical and mechanical properties of WSCF coatings, due to the doping with F and C.

Based on the results of the nanoindentation test, WSCF1 showed the highest hardness. Thus, it can be deduced the high hardness, and stronger interlayer bonds in the structure prevent the presence of adherent materials on the sliding surface of the ball. Consequently, the more problematic formation of the tribolayer for WSCF1 coating increased the friction coefficient between the sliding surfaces. Regarding the optical images of wear track, while surfaces appear rather smooth and worn uniformly over the contact, zones with different aspect can be detected inside the wear track. These zones can contain other elements, including Cr from the interlayer or Fe from the counterpart ball because of the lower thickness in those areas.

Fig. 31 offers an overall view of how the sputtered surfaces behaved during the tribotest. For the WS_x-based TMD coatings, it is not necessarily that high friction results in high wear rate, because these coatings are soft and can be easily sheared to show low COF but give high wear. This property entails the use of WS_x-based materials used as a coating in dry conditions. It has previously been reported that the presence of a tribofilm may be sufficient to sustain low friction even at the removal of the original thin film [9][72].
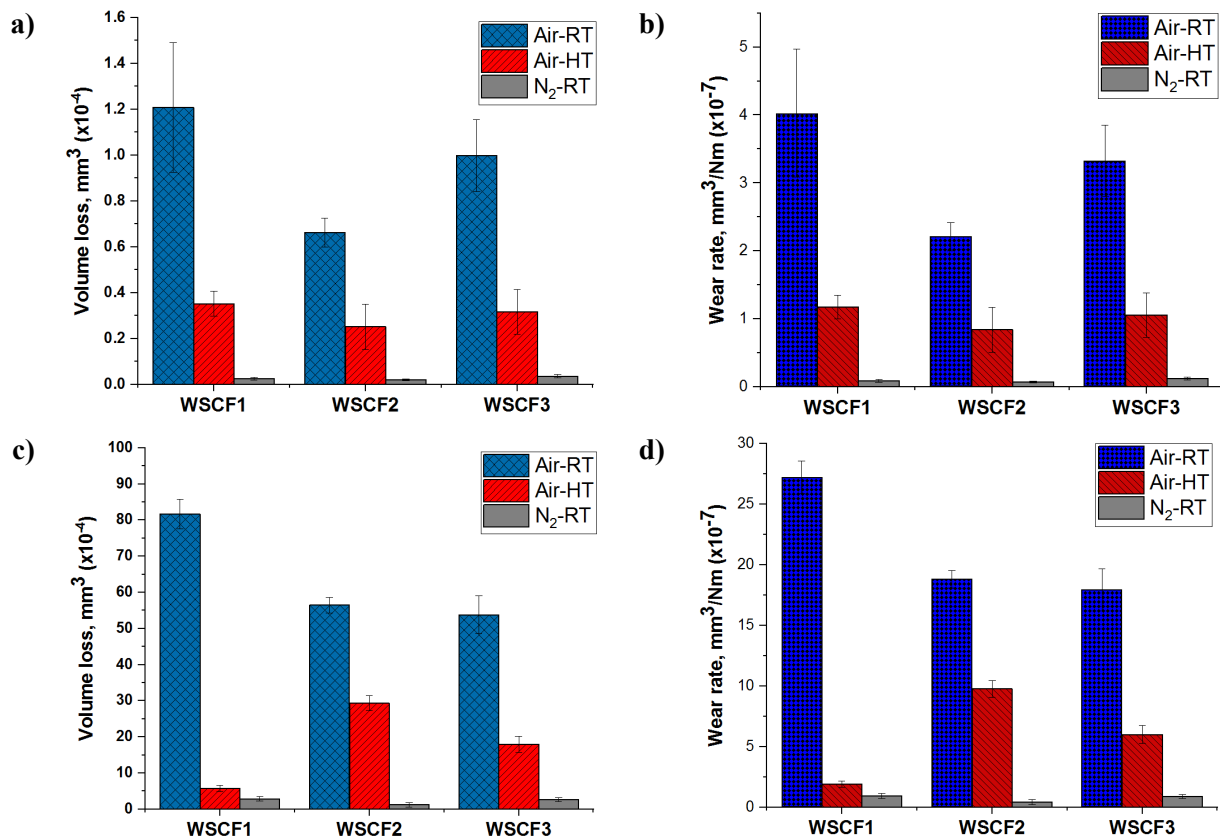

Figure 31: Volume loss and wear rate for balls (a and b), and discs (c and d) after the wear test.

Comparison of volume loss and wear rate of the balls after 600 s SRV tests show that their trends align well with the COF trends, i.e. the counterpart ball in the SRV test of WSCF2 have a lower volume loss, wear rate and COF than WSCF3, while WSCF1 showed the highest values for these tribological parameters. On the contrary, the trends above for the stationary discs were completely different, except the wear rate and volume loss values at dry N_2 condition. These values, however, expectedly decreased at 200 °C for WSCF2 and WSCF3 while showing very low values for WSCF1 despite previous trends for balls.

The observation of the coatings tribological behaviour reveals that more F content in the coating decreased the wear resistance of the sputtered discs at a higher temperature, which can be due to the higher diffusion and segregation of F atoms in the structure.

The optical images and calculated wear depth reveal the chromium interlayer and the substrate were reached at Air-RT and Air-HT, which confirm the assumption that the coatings were partially removed during the SRV test. From the results of SRV tests at elevated temperature, it could be concluded that high temperature would favour the transfer layer formation. These observations agree with Sundberg et al. who reported that TMDs have proven to work excellent at a higher temperature, not only because of tribolayer formation but also due to the removal of adsorbed water [91].

At dry condition (N_2), the wear volume and rate values for the sputtered discs showed more or less the same tribological behaviour as the balls. Obtaining wear profiles for all coatings at dry conditions were challenging as these coatings have good solid lubricity properties and are not worn out throughout the tribotest. The low wear resistance of the WSCF films corresponds to the strong detachment of wear debris, which is mainly composed of Fe and W oxides and residues of W-S material. According to the literature, the wear resistance of WSCF coatings is generally better than single WS thin film, due to the higher hardness of these coatings compared to WS [42].

Chapter 5 - Conclusions

In this study, a series of WSCF solid lubricants have been deposited by reactive magnetron sputtering. The coatings characterised by several experimental techniques to investigate the effects of alloying WS_x-based coating via C and F on the microstructural, mechanical and tribological properties of the films. In order to gain an understanding of the tribological behaviour of the coatings under dry and lubricated conditions, the coatings were studied at dry (exposed to N_2 flow at room temperature) and lubricated conditions by the humidity of the air at two temperatures: room temperature and 200 °C. This chapter presents the main conclusions of this study.

❖ The effects of alloying C and F elements on the microstructural of sputter-deposited WSCF coatings have been investigated, and the main results are as follows:

- From the SEM results, it can be seen the morphology of the films is the typical cauliflower-like structure at the scale of lower than 100 nm. The cross-sectional view showed a quite compact and columnar structure, where WSCF3 and WSCF2 were more homogeneous than WSCF1. For a higher amount of C in the structure, the coatings became denser, thicker, as well as with a lower number of fissures and agglomeration sites on the surface. The thickness of the coatings was between 1.702 to 1.911 μm, including a chromium interlayer thickness of 0.272-0.304 μm. The increase of the alloying element contents resulted in a featureless morphology with a lower level of porosity and higher compactness. In particular, increasing C contents indicated the improvement of the morphology of films.

  Based on the WDS results, it is revealed higher applied power on C cathodes increased the carbon contents of the film, while W and S were decreased. It is revealed with the increase of the power on the C targets there was a significant reduction of the O content in the films. There was no direct relationship between increasing C contents and the concentration of F in the coatings. It seems that the O is replacing the F when the C targets are not working. To explain why WSCF1 showed more oxygen, it can be noted that since it was less compacted than the other two samples with a higher amount of alloying elements, it is more likely adsorbed contaminants like oxygen.

- XRD patterns showed four characteristic peaks of the hexagonal WS_2 and two peaks indexed as Si and Cr for all coatings. In addition, an extended shoulder as a feature of turbostratic stacking of S-W-S single layers was observed in all samples. The weak interactions between two S-W-S layers cause rotational and/or translational disorder around the c axis, relative to each other. This phenomenon plays the main role in the solid lubricity of these coatings. With the additional source of C from the targets, the coatings became amorphous. XRD patterns suggested that the coating becomes amorphous for a C and F contents of over 15.5 and 9.3 at. %, respectively. The increasing diffusivity of the alloying atoms in the WSCF coatings may explain the difference in crystallinity between pure and alloyed WS_x TMDs.

- According to the AFM results, the same behaviour in height ranges of backward and forward images confirmed the presence of adhesive force is neglectable. As it can be seen from the 3D AFM images, the morphology of the coating is cauliflower with lots of small rounds–shape structures on the surface, which was confirmed by SEM images. Based on the measured roughness values, the highest amount of carbon in the coating led to much smoother surfaces.

43

❖ Mechanical analysis of the coatings confirmed the following results:

▪ Nanoindentation suggested that the hardness of coatings is in the same range, however, the WSCF2 had the lowest hardness, and this coating represented the highest reduced Young's modulus. It means that while higher F incorporation in the structure reduced the hardness slightly, the Reduced Young's modulus is not changed linearly by alloying of WS_x-based coatings in this research.

▪ Regarding adhesion tests, the addition of F did not have a linear effect on the L_{C2} values, whereas more carbon in the coating increased the failure load values. The agreement between higher L_{C2} values and the C content in WSCF3 coating suggested that the higher C content and more compactness improved the adhesion behaviour of this coating.

❖ In order to investigate the influence of the alloying contents on the tribological behaviour of coatings, tribotests were conducted in an SRV instrument led to the results below:

▪ All WSCF coatings tested for 600 s presented the average COF in the range from 0.008 to 0.071, maintaining low COF for suitable solid lubricity. The general trend of decrease in friction coefficient with increasing the alloying elements is attributed to the theory that more C and F in the coating can ease the crystalline slipping of the basal planes that are weakly bonded to each other with the van der Waals force. Despite the significant difference in the COF trends, the obtained values of the coefficient of friction indicate the overall solid-lubrication behaviour for every sample at each condition were likely similar together. The lubrication performance of the thin films remained in the best condition in the dry environment. In contrast, the aggressive condition of Air-HT environment led to a faster COF increasing compared to the Air-RT and N_2 for all three coatings because of the coatings removal or partial removal at the contact area with the ball counterpart. As the hexagonal structure is expanded by insertion of the fluorine on the WS_2 lattice, the van der Waals bonding energy between the layers is decreased. Accordingly, it can explain why the calculated friction from tribological tests for WSCF2 (with the highest amount of F) is lower than WSCF1 and WSCF3 at both lubricated (%Rh of 35%) and dry conditions. The weaker van der Waals bonds in the surface due to more fluorine incorporation in the S-W-S layers are the main reason for lower COF for WSCF2. Furthermore, the F can prevent WS_2 oxidation by withdrawing more electron density than oxygen attaching to high energy sites in the W_z non-bonding orbital, which result in the easy shear ability of the tribofilm. At elevated temperature, however, a higher amount of alloying elements in the structure can increase the friction force, possibly through accelerating the oxidation by a high amount of carbon.

▪ The high hardness and stronger interlayer bonds in the structure prevent the presence of adherent materials on the sliding surface of the ball. Consequently, the more problematic formation of the tribolayer for WSCF1 coating increased the friction coefficient and wear rate between the sliding surfaces. Comparison of volume loss and wear rate for the balls shows that their trends align well with the COF trends. On the contrary, the trends above for the stationary discs were completely different, showing very low values for WSCF1 despite previous trends for balls. It means more F content in the coating decreased the wear resistance of the sputtered discs at a higher temperature, which can be due to the higher diffusion and segregation of F atoms in the structure. The low wear resistance of the WSCF films corresponds to the strong detachment of wear debris, which is mainly composed of Fe and W oxides and residues of W-S material. However, the wear resistance of WSCF coatings is generally better than single WS thin film studied in the literature, due to the higher hardness of these coatings compared to WS.

Future work

In short, this work established an important basis for the future works on WSCF, which could focus on:

(1) Investigation of increasing the F with further increase the CF4 flow keeping the O content as low as in the coatings deposited with a power on the C targets.

(2) The improvement of the coating process to decrease the amount of oxides to achieve better thin films.

(3) Heat treatment of these coatings in order to enhance their amorphous structure.

(4) Conducting a new set of experiments including wettability, corrosion tests and tribocorrosion study, as well as using oil-based lubricants, to expand the knowledge of WSCF coatings.

Bibliography

[1]   Holmberg, Kenneth, and Ali Erdemir. "The impact of tribology on energy use and CO_2 emission globally and in combustion engine and electric cars." Tribology International 135 (2019): 389-396.

[2]   Stachowiak, Gwidon, and Andrew W. Batchelor. Engineering tribology. Butterworth-Heinemann, 2013.

[3]   Holmberg, Kenneth, Peter Andersson, Nils-Olof Nylund, Kari Mäkelä, and Ali Erdemir. "Global energy consumption due to friction in trucks and buses." Tribology International 78 (2014): 94-114.

[4]   Tabor, David. "Friction—the present state of our understanding." Journal of lubrication technology 103, no. 2 (1981): 169-179.

[5]   Rabinowicz, Ernest. "The determination of the compatibility of metals through static friction tests." ASLE Transactions 14, no. 3 (1971): 198-205.

[6]   Scharf, T. W., and S. V. Prasad. "Solid lubricants: a review." Journal of materials science 48, no. 2 (2013): 511-531.

[7]   Muratore, Christopher, and Andrey A. Voevodin. "Chameleon coatings: adaptive surfaces to reduce friction and wear in extreme environments." Annual Review of Materials Research 39 (2009): 297-324.

[8]   Pimentel, João Vitor Bernardo. "Adaptive self-lubricating low-friction coatings." (2013).

[9]   Sundberg, Jill. "Trioactive Low-Friction Coatings Based on Sulfides and Carbides." PhD diss., Acta Universitatis Upsaliensis, 2014.

[10]   Aouadi, Samir M., Hongyu Gao, Ashlie Martini, Thomas W. Scharf, and Christopher Muratore. "Lubricious oxide coatings for extreme temperature applications: A review." Surface and Coatings Technology 257 (2014): 266-277.

[11]   Arif, Aditya F., Ratna Balgis, Takashi Ogi, Ferry Iskandar, Akihiro Kinoshita, Keitaro Nakamura, and Kikuo Okuyama. "Highly conductive nano-sized Magnéli phases titanium oxide (TiO$_x$)." Scientific reports 7, no. 1 (2017): 3646.

[12]   Smith, J. R., F. C. Walsh, and R. L. Clarke. "Electrodes based on Magnéli phase titanium oxides: the properties and applications of Ebonex materials." Journal of applied electrochemistry 28, no. 10 (1998): 1021-1033.

[13]   Tedstone, Aleksander A., David J. Lewis, and Paul O'Brien. "Synthesis, properties, and applications of transition metal-doped layered transition metal dichalcogenides." Chemistry of Materials 28, no. 7 (2016): 1965-1974.

[14]   Niederhäuser, P., H. E. Hintermann, and M. Maillat. "Moisture-resistant MoS$_2$-based composite lubricant films." Thin Solid Films 108, no. 2 (1983): 209-218.

[15]   Zabinski, J. S., J. E. Florkey, S. D. Walck, J. E. Bultman, and N. T. McDevitt. "Friction properties of WS$_2$/graphite fluoride thin films grown by pulsed laser deposition." Surface and Coatings Technology 76 (1995): 400-406.

[16]   John, P. J., S. V. Prasad, A. A. Voevodin, and J. S. Zabinski. "Calcium sulfate as a high temperature solid lubricant." Wear 219, no. 2 (1998): 155-161.

[17]   Xiao, Huaping, and Shuhai Liu. "2D nanomaterials as lubricant additive: A review." Materials & Design 135 (2017): 319-332.

[18]   Prajapati, Ajay Kumar, Emad Omrani, Pradeep L. Menezes, and Pradeep K. Rohatgi. "Fundamentals of Solid Lubricants." In Self-Lubricating Composites, pp. 1-32. Springer, Berlin, Heidelberg, 2018.

[19]   Sorkin, V., H. Pan, H. Shi, S. Y. Quek, and Y. W. Zhang. "Nanoscale transition metal dichalcogenides: structures, properties, and applications." Critical Reviews in Solid State and Materials Sciences 39, no. 5 (2014): 319-367.

[20]   Watanabe, S., J. Noshiro, and S. Miyake. "Tribological characteristics of WS_2/MoS_2 solid lubricating multilayer films." Surface and Coatings Technology 183, no. 2-3 (2004): 347-351.

[21]   Brown, S., J. L. Musfeldt, I. Mihut, J. B. Betts, A. Migliori, A. Zak, and R. Tenne. "Bulk vs nanoscale WS_2: finite size effects and solid-state lubrication." Nano letters 7, no. 8 (2007): 2365-2369.

[22]   He, Xingliang, Huaping Xiao, Hyunho Choi, Agustín Díaz, Brian Mosby, Abraham Clearfield, and Hong Liang. "α-Zirconium phosphate nanoplatelets as lubricant additives." Colloids and Surfaces A: Physicochemical and Engineering Aspects 452 (2014): 32-38.

[23]   Miyoshi, Kazuhisa. "Solid lubricants and coatings for extreme environments: state-of-the-art survey." (2007).

[24]   Prajapati, Ajay Kumar, Emad Omrani, Pradeep L. Menezes, and Pradeep K. Rohatgi. "Fundamentals of Solid Lubricants." In Self-Lubricating Composites, pp. 1-32. Springer, Berlin, Heidelberg, 2018.

[25]   Watanabe, S., J. Noshiro, and S. Miyake. "Tribological characteristics of WS_2/MoS_2 solid lubricating multilayer films." Surface and Coatings Technology 183, no. 2-3 (2004): 347-351.

[26]   Pumera, Martin, Zdeněk Sofer, and Adriano Ambrosi. "Layered transition metal dichalcogenides for electrochemical energy generation and storage." Journal of Materials Chemistry A 2, no. 24 (2014): 8981-8987.

[27]   Li, Henan, Yumeng Shi, Ming-Hui Chiu, and Lain-Jong Li. "Emerging energy applications of two-dimensional layered transition metal dichalcogenides." Nano Energy 18 (2015): 293-305.

[28]   Xia, Dawei David, Feng Gong, Xudong Pei, Wenbin Wang, Hao Li, Wei Zeng, Mengqiang Wu, and Dimitrios V. Papavassiliou. "Molybdenum and tungsten disulfides-based nanocomposite films for energy storage and conversion: A review." Chemical Engineering Journal (2018).

[29]   Xu, Jing, Linjian Dong, Hua Tang, and Changsheng Li. "Facile synthesis of Mo0. 91W0. 09S2 ultrathin nanosheets/amorphous carbon composites for lithium-ion battery anode." Ceramics International 42, no. 6 (2016): 7803-7809.

[30]   Castellanos-Gomez, Andres, Menno Poot, Gary A. Steele, Herre SJ van der Zant, Nicolás Agraït, and Gabino Rubio-Bollinger. "Elastic properties of freely suspended MoS_2 nanosheets." Advanced Materials 24, no. 6 (2012): 772-775.

[31]   Peng, Qing, Wei Ji, and Suvranu De. "Mechanical properties of the hexagonal boron nitride monolayer: Ab initio study." Computational Materials Science 56 (2012): 11-17.

[32]   Lee, Changgu, Xiaoding Wei, Jeffrey W. Kysar, and James Hone. "Measurement of the elastic properties and intrinsic strength of monolayer graphene." science 321, no. 5887 (2008): 385-388.

[33]   Lindahl, Niklas, Daniel Midtvedt, Johannes Svensson, Oleg A. Nerushev, Niclas Lindvall, Andreas Isacsson, and Eleanor EB Campbell. "Determination of the bending rigidity of graphene via electrostatic actuation of buckled membranes." Nano letters 12, no. 7 (2012): 3526-3531.

[34]   Yun, Qinbai, Qipeng Lu, Xiao Zhang, Chaoliang Tan, and Hua Zhang. "Three-Dimensional Architectures Constructed from Transition-Metal Dichalcogenide Nanomaterials for Electrochemical Energy Storage and Conversion." Angewandte Chemie International Edition 57, no. 3 (2018): 626-646.

[35]   Mutafov, Petr, Manuel Evaristo, Albano Cavaleiro, and Tomas Polcar. "Structure, mechanical and tribological properties of self-lubricant W–S–N coatings." Surface and Coatings Technology 261 (2015): 7-14.

[36]   Polcar, Tomas, and Albano Cavaleiro. "Self-adaptive low friction coatings based on transition metal dichalcogenides." Thin Solid Films 519, no. 12 (2011): 4037-4044.

[37]   Polcar, T. Self-lubricating nanostructured coatings based on transition metal dichalcogenides alloyed with carbon. Habilitation thesis, Czech Technical University in Prague, 2009.

[38]   Gustavsson, Fredrik, Staffan Jacobson, Albano Cavaleiro, and Tomas Polcar. "Ultra-low friction W–S–N solid lubricant coating." Surface and Coatings Technology 232 (2013): 541-548.

[39] Voevodin, A. A., and J. S. Zabinski. "Supertough wear-resistant coatings with 'chameleon'surface adaptation." Thin Solid Films 370, no. 1-2 (2000): 223-231.

[40] Nossa, A., and A. Cavaleiro. "Mechanical behaviour of W–S–N and W–S–C sputtered coatings deposited with a Ti interlayer." Surface and Coatings Technology 163 (2003): 552-560.

[41] Chen, Zhe, Xin He, Chen Xiao, and Seong Kim. "Effect of Humidity on Friction and Wear—A Critical Review." Lubricants 6, no. 3 (2018): 74.

[42] Rodrigues, S. P., M. Evaristo, S. Carvalho, and A. Cavaleiro. "Fluorine-carbon doping of WS-based coatings deposited by reactive magnetron sputtering for low friction purposes." Applied Surface Science 445 (2018): 575-585.

[43] Shi, Q., H. Tang, H. Zhu, G. Tang, K. Zhang, H. Zhang, and C. Li. "Synthesis and tribological properties of Ti-doped NbSe 2 nanoparticles." Chalcogenide Letters 11, no. 5 (2014).

[44] Soto-Castillo, Roger G., Girija S. Chaubey, and George Diloyan. "Industrial lubricant including metal chalcogenide particles and phosphorus-based additive." U.S. Patent Application 15/204,541, filed January 12, 2017.

[45] Singh, Harpal, K. C. Mutyala, H. Mohseni, T. W. Scharf, R. D. Evans, and G. L. Doll. "Tribological performance and coating characteristics of sputter-Deposited Ti-Doped MoS₂ in rolling and sliding contact." Tribology Transactions 58, no. 5 (2015): 767-777.

[46] Cammarata, Antonio, and Tomáš Polcar. "Tailoring nanoscale friction in MX2 transition metal dichalcogenides." Inorganic chemistry 54, no. 12 (2015): 5739-5744.

[47] Lian, Yunsong, Jianxin Deng, Shipeng Li, Guangyuan Yan, and Shuting Lei. "Friction and wear behavior of WS 2/Zr self-lubricating soft coatings in dry sliding against 40Cr-hardened steel balls." Tribology Letters 53, no. 1 (2014): 237-246.

[48] Polcar, T., and A. Cavaleiro. "Review on self-lubricant transition metal dichalcogenide nanocomposite coatings alloyed with carbon." Surface and Coatings Technology 206, no. 4 (2011): 686-695.

[49] Kogovšek, J., and M. Kalin. "Various MoS 2-, WS 2-and C-based micro-and nanoparticles in boundary lubrication." Tribology Letters 53, no. 3 (2014): 585-597.

[50] Schmidt, Susann, Grzegorz Greczynski, Cecilia Goyenola, Gueorgui Kostov Gueorguiev, Zs Czigány, Jens Jensen, Ivan Gueorguiev Ivanov, and Lars Hultman. "CFx thin solid films deposited by high power impulse magnetron sputtering: Synthesis and characterization." Surface and Coatings Technology 206, no. 4 (2011): 646-653.

[51] Wang, Qing Hua, Kourosh Kalantar-Zadeh, Andras Kis, Jonathan N. Coleman, and Michael S. Strano. "Electronics and optoelectronics of two-dimensional transition metal dichalcogenides." Nature nanotechnology 7, no. 11 (2012): 699.

[52] Mattox, Donald M. Handbook of physical vapor deposition (PVD) processing. William Andrew, 2010.

[53] Djugum, Richard. Novel fabrication processes for thin film vapour deposited strain gauges on mild steel. Swinburne University of Technology, School of Engineering and Science, 2006.

[54] Kim, Sung-Hwa, and Chang Kwon Hwangbo. "Influence of Ar ion-beam assistance and annealing temperatures on properties of TiO2 thin films deposited by reactive DC magnetron sputtering." Thin Solid Films 475, no. 1-2 (2005): 155-159.

[55] Garrison Jr, W. M. "Steels: classifications." (2001): 8840-8843.

[56] Goldstein, Joseph I., Dale E. Newbury, Joseph R. Michael, Nicholas WM Ritchie, John Henry J. Scott, and David C. Joy. Scanning electron microscopy and X-ray microanalysis. Springer, 2017.

[57] Reimer, Ludwig. Scanning electron microscopy: physics of image formation and microanalysis. Vol. 45. Springer, 2013.

[58] Brady, John B., and Shelby J. Boardman. "Introducing mineralogy students to x-ray diffraction through optical diffraction experiments using lasers." Journal of Geological Education 43, no. 5 (1995): 471-476.

[59] Cole, H. "Bragg's law and energy sensitive detectors." Journal of Applied Crystallography 3, no. 5 (1970): 405-406.

[60] Birkholz, Mario. Thin film analysis by X-ray scattering. John Wiley & Sons, 2006.

[61] Madsen, Ian C., Nicola VY Scarlett, and Arndt Kern. "Description and survey of methodologies for the determination of amorphous content via X-ray powder diffraction." Zeitschrift für Kristallographie Crystalline Materials 226, no. 12 (2011): 944-955.

[62] Stabrawa, I., A. Kubala-Kukuś, D. Banaś, G. Pepponi, J. Braziewicz, M. Pajek, and M. Teodorczyk. "Characterization of the morphology of titanium and titanium (IV) oxide nanolayers deposited on different substrates by application of grazing incidence X-ray diffraction and X-ray reflectometry techniques." Thin Solid Films 671 (2019): 103-110.

[63] P. Scherrer , "Bestimmung der Grosse und der inneren Struktur von Kolloidteilchen mittels Rontgenstrahlen/' Nachr. Ges. Wiss. Góttingen 26 (1918) pp 98-100.

[64] Payton, O., A. R. Champneys, M. E. Homer, L. Picco, and M. J. Miles. "Feedback-induced instability in tapping mode atomic force microscopy: theory and experiment." Proceedings of the Royal Society A: Mathematical, Physical and Engineering Sciences 467, no. 2130 (2010): 1801-1822.

[65] Beckman Institute for Advanced Science and Technology, University of Illinois at Urbana-Champaign. "AFM tutorial". http://virtual.itg.uiuc.edu/training/AFM_tutorial/ (accessed May 1, 2019)

[66] Korayem, M. H., A. Kavousi, and N. Ebrahimi. "Dynamic analysis of tapping-mode AFM considering capillary force interactions." Scientia Iranica 18, no. 1 (2011): 121-129.

[67] Callisti, M. "Microstructural and nanomechanical characterisation of Ni-Ti (-Cu) shape memory alloy thin films for tribology." PhD diss., University of Southampton, 2014.

[68] Fischer-Cripps, Anthony C. "Critical review of analysis and interpretation of nanoindentation test data." Surface and coatings technology 200, no. 14-15 (2006): 4153-4165.

[69] Hogmark, Sture, Staffan Jacobson, and Mats Larsson. "Design and evaluation of tribological coatings." Wear 246, no. 1-2 (2000): 20-33.

[70] Franz, R., J. Schnöller, H. Hutter, and C. Mitterer. "Oxidation and diffusion study on AlCrVN hard coatings using oxygen isotopes 16O and 18O." Thin Solid Films 519, no. 12 (2011): 3974-3981.

[71] Ramana, C. V. "Properties of sputter-deposited gallium oxide." In Gallium Oxide, pp. 47-66. Elsevier, 2019.

[72] Gustavsson, Fredrik. "Trioactive Component Coatings: Tribological Testing and Microanalysis of Low-Friction Tribofilms." PhD diss., Acta Universitatis Upsaliensis, 2013.

[73] Oliver, W. C., and Pharr, G. M., 1992, "An improved technique for determining hardness and elastic modulus using load and displacement sensing indentation experiments," J. Mater. Res., 7(06), pp. 1564–1583.

[74] Antunes, J. M., A. Cavaleiro, L. F. Menezes, M. I. Simoes, and J. V. Fernandes. "Ultra-microhardness testing procedure with Vickers indenter." Surface and Coatings Technology 149, no. 1 (2002): 27-35.

[75] Mittal, Ed KL. "Scratch adhesion testing of coated surfaces-Challenges and new directions." (2001).

[76] Camino, D., D. G. Teer, J. Von Stebut, M. G. Gee, N. M. Jennett, J. Banks, B. Bellaton, E. Matthaei-Schulz, and H. Vetters. "Scratch adhesion testing of coated surfaces-Challenges and new directions." Adhesion Measurement of Films & Coatings: Volume 2 2 (2001): 79.

[77] Kopeliovich, Dmitri, "Adhesion tests", http://www.substech.com/dokuwiki/doku.php?id=adhesion_tests (accessed May 1, 2019)

[78] Aldrich-Smith, G., N. Jennett, and J. Housden. "A round robin to measure the adhesion of thin coatings." VAMAS TWA 22 (2004).

[79] Ingelbrecht, C., Jennett, N., Jacobs, R., & Meneve, J. "The certification of critical coating failure loads : a reference material for scratch testing according to ENV 1071-3" 1994 BCR-692 (2006).

[80] Rabinowicz, Ernest. "Friction and Wear of Materials, Jhon Wiley & Sons." Inc., New York (1995).

[81] Briant, Jean, and Jean-Claude Hipeaux. Lubricant properties analysis & testing. Editions Technip, 2000.

[82]   ASTM D5707-16, Standard Test Method for Measuring Friction and Wear Properties of Lubricating Grease Using a High-Frequency, Linear-Oscillation (SRV) Test Machine, ASTM International, West Conshohocken, PA, 2016.

[83]   Hardell, Jens, and Braham Prakash. "High-temperature friction and wear behaviour of different tool steels during sliding against Al–Si-coated high-strength steel." Tribology International 41, no. 7 (2008): 663-671.

[84]   Polcar, T., M. Evaristo, and A. Cavaleiro. "The tribological behavior of W–S–C films in pin-on-disk testing at elevated temperature." Vacuum 81, no. 11-12 (2007): 1439-1442.

[85]   Nossa, A., and A. Cavaleiro. "Chemical and physical characterization of C (N)-doped W–S sputtered films." Journal of materials research 19, no. 8 (2004): 2356-2365.

[86]   Evaristo, M., A. Nossa, and A. Cavaleiro. "W–S–C sputtered films: Influence of the carbon alloying method on the mechanical properties." Surface and Coatings Technology 200, no. 1-4 (2005): 1076-1079.

[87]   Regula, M., C. Ballif, J. H. Moser, and F. Levy. "Structural, chemical, and electrical characterisation of reactively sputtered WS_x thin films." Thin Solid Films 280, no. 1-2 (1996): 67-75.

[88]   Nossa, A., and A. Cavaleiro. "The influence of the addition of C and N on the wear behaviour of W–S–C/N coatings." Surface and Coatings Technology 142 (2001): 984-991.

[89]   Machlin, Eugene. Materials science in microelectronics II: the effects of structure on properties in thin films. Vol. 2. Elsevier, 2010.

[90]   International Centre for Diffraction Data (ICCD), Pensylvania. ficha 00-002-0131.

[91]   Sundberg, Jill, Harald Nyberg, Erik Särhammar, Tomas Nyberg, Staffan Jacobson, and Ulf Jansson. "Influence of composition, structure and testing atmosphere on the tribological performance of W–S–N coatings." Surface and Coatings Technology 258 (2014): 86-94.

[92]   Moser, J., and F. Levy. "MoS_2− x lubricating films: structure and wear mechanisms investigated by cross-sectional transmission electron microscopy." Thin Solid Films 228, no. 1-2 (1993): 257-260.

[93]   Zhang, Guangqiang, Yue Xu, Dapeng Xu, Deyong Wang, Yanfeng Xue, and Wenhui Su. "Pressure-induced crystallization of amorphous SiO2 with silicon–hydroxy group and the quick synthesis of coesite under lower temperature." High Pressure Research 28, no. 4 (2008): 641-650.

[94]   Nossa, A., Cavaleiro, A. Characterization of WS_x sputtered films. Actas "Materials 99, Universidade do Minho, 1, 1999.

[95]   Ricci, Davide, and Pier Carlo Braga. "Recognizing and avoiding artifacts in AFM imaging." In Atomic Force Microscopy, pp. 25-37. Humana Press, 2004.

[96]   Xu, Jiao, Liqiang Chai, Li Qiao, Tengfei He, and Peng Wang. "Influence of C dopant on the structure, mechanical and tribological properties of rf-sputtered MoS_2/aC composite films." Applied Surface Science 364 (2016): 249-256.

[97]   Pei, Y. T., D. Galvan, J. Th M. De Hosson, and A. Cavaleiro. "Nanostructured TiC/aC coatings for low friction and wear resistant applications." Surface and Coatings Technology 198, no. 1-3 (2005): 44-50.

[98]   Kim, Seock-Sam, Chan-Wook Ahn, and Tae-Hyung Kim. "Tribological characteristics of magnetron sputtered MoS_2 films in various atmospheric conditions." KSME international journal 16, no. 9 (2002): 1065-1071.

[99]   Pimentel, J. V., T. Polcar, M. Evaristo, and A. Cavaleiro. "Examination of the tribolayer formation of a self-lubricant W–S–C sputtered coating." Tribology International 47 (2012): 188-193.

[100]   Fleischauer, Paul D., Jeffrey R. Lince, P. A. Bertrand, and Reinhold Bauer. "Electronic structure and lubrication properties of molybdenum disulfide: a qualitative molecular orbital approach." Langmuir 5, no. 4 (1989): 1009-1015.

[101]   Polcar, T., and A. Cavaleiro. "Review on self-lubricant transition metal dichalcogenide nanocomposite coatings alloyed with carbon." Surface and Coatings Technology 206, no. 4 (2011): 686-695.

Appendix
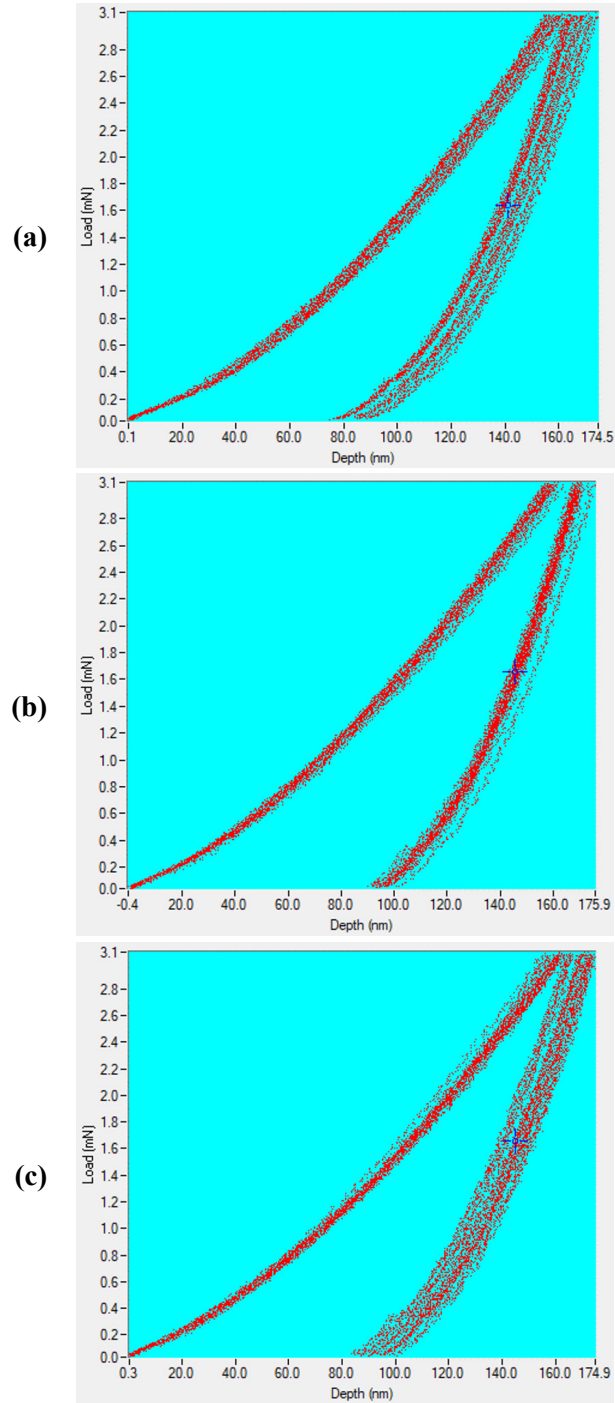
Nanoindentation load-displacement curves

Figure A.1: Nanoindentation load-displacement curves for as-deposited films: (a) WSCF1, (b) WSCF2, and (c) WSCF3.